Contents lists available at ScienceDirect

Applied Surface Science

Full Length Article

The hinge morphology of SnO$_2$ as multifunctional semiconductor: What we can learn from simulations, theory, and experiments

Amanda F. Gouveia [a,*], Celso M. Aldao [b], Miguel A. Ponce [c], Edson R. Leite [d,e], Elson Longo [e], Juan Andrés [a,d]

[a] *Department of Analytical and Physical Chemistry, University Jaume I (UJI), Castelló 12071, Spain*
[b] *Institute of Scientific and Technological Research in Electronics (ICYTE), University of Mar del Plata and National Research Council (CONICET), Juan B. Justo 4302, B7608FDQ Mar del Plata, Argentina*
[c] *Institute of Materials Science and Technology (INTEMA), University of Mar del Plata and National Research Council (CONICET), Mar del Plata B7608FDQ, Argentina*
[d] *Brazilian Nanotechnology National Laboratory (LNNano), CNPEM, 13083-970 Campinas, SP, Brazil*
[e] *Center for the Development of Functional Materials (CDMF), Federal University of São Carlos, São Carlos, SP, Brazil*

ARTICLE INFO

ABSTRACT

Our interaction with materials occurs through their surfaces whose properties are strongly dependent on morphology, structure, and atomic arrangement. Unfortunately, obtaining a detailed correlation between the surface morphology with its properties is not straightforward. SnO$_2$ is a multifunctional semiconductor ceramic that is exploited in several technological devices from sensor to energy storage, water splitting, and solar to fuel photocatalysis. This work focused on the structural, energetic, and electronic properties of low and high index surfaces of SnO$_2$ semiconductor and assessed the morphology-dependent process via first-principles calculations, at the density functional theory level. Importantly, our explicitly dynamic approach elucidates the atomic arrangements and stability of the exposed surfaces to provide a close match between experimental field emission scanning electron microscopy images and computational simulation. These findings can potentially set a foundation for establishing synthesis techniques for drive the morphology evolution through the control of temperature/pressure, and/or based on surface interactions of the selective adsorption of solvents/surfactants.

1. Introduction

The crystal structure and morphology of the multifunctional semiconductors are the most important characteristics that dictates its physical–chemical properties, for properties directly related to the surface. Crystal facet engineering is an important issue in inorganic materials that provides the control of morphology, composition, structure, and atomic arrangement, endowing them with distinct and intensified development of technological applications (in optics, sensor, catalytic, photocatalysis, and so on) [1–6].

The specific atomic configurations at the surface of metal oxides, i.e., the local coordination of the exposed cations (clusters), have a very significant effect on the surface chemistry [7–10] responsible for the formation of reactive oxygen species and their interaction with possible adsorbates and microorganisms, involved in the photocatalytic and biocide activity, respectively. However, it has been a challenge to

explicitly understand both the surface configuration and the structure-dependent properties, at the atomic level, due to their complex nature. Therefore, a complete understanding of the structural, energetic, and electronic differences between the exposed surfaces at the morphology is essential to identifying (the best suited surface for different desired applications) which surface is best suited as a desired application. Atoms located at the surface of solids are undercoordinated, comparing with bulk atoms, thus they are the active sites where the corresponding chemical/physical process, i.e., sensor activity, adsorption of molecules from the environment, chemical reactions, and so on, take place.

Since the adsorption and desorption of molecules depend strictly on the surface atomic arrangement, different orientations result in distinct local properties and provide different catalytic activities and chemical reactivity [11]. In particular, the sensing mechanism is controlled by the structure and the electronic properties of the sensor surfaces where the chemical reactions are carried out, which are highly dependent on the

exposed surface [12–15]. With the development of advanced electron microscopy, impressive images can, in principle, be gained at atomic spatial scale [16]. However, the evolution of the morphology and exposed surfaces of materials is sensitive to experimental conditions such as temperature and gaseous type and pressure, which brings about a great experimental challenge to obtain this information. On the other hand, first-principles calculations based on the density functional theory (DFT) provide a versatile method that makes up for the lack or complement of experimental surface studies. The combination of both tools has the advantage of identifying the corresponding atomic and electronic structures and has great potential in exploring the underlying activity. Consequently, establishing realistic and reliable material surface models is undoubtedly the first step and the most important link connecting the images of the morphology provided by advanced field emission scanning electron microscopy (FE-SEM) and theoretical calculations [17].

Tin dioxide (SnO$_2$) based materials have attracted comprehensive interest for their wide range of functional applications due to the *n*-type wide band gap (3.6 eV at 300 K) [18], high charge carrier density, stable crystal structure, controllable vacancies sites creation, and abundant chemical properties [19,20]. The formation of SnO$_2$, as in any inorganic oxide, involves three processes: nucleation, growth, and morphology evolution. Among them, the latter is less understood because the morphology of SnO$_2$-based materials depends on several factors which include synthesis method and reaction conditions such as solvents, surfactant, temperature, and so on. These factors are responsible for the change in growth of different morphologies of SnO$_2$-based materials and some of them are shown in Fig. 1.

1.1. How SnO$_2$ works as a gas sensor?

Metal semiconductor oxides have been widely studied as gas sensors for the selective detection of various gases with trace concentrations. The identification of the reaction mechanism associated to the gas sensing response is crucial for further development; however, the mechanism of gas sensing is still controversial. The current state of knowledge of the gas sensing mechanism of metal oxides is based on the modulation of the conductivity of active materials through the formation/removal of surface O-related acceptors. However, the exact nature of species behind the sensing response remains obscure and their characterization at the surface reactions are more difficult than initially assumed [27,28]. It is very important to highlight that the electronic conduction mechanisms are affected not only by the nature of the semiconductor but also by the specific exposed surfaces of the material that determine the type and amount of adsorbed oxygen.

SnO$_2$, as a gas sensor, detects changes in a gaseous atmosphere due to variations in electrical resistance. This arises from charge transfer due to chemical interaction at gas–solid interfaces. The chemical interaction between the adsorbed gas and the semiconductor surface modifies the charge density at the semiconductor, directly impacting the material's charge transport. The semiconductor gas sensor relies on the receptor function and the transducer function to generate the gas-sensing response. The receptor function is related to how the sensor recognizes or identifies chemical substances such as gas molecules, and the transducer function concerns how the sensor converts chemical signals into output signals [29–32]. This property is due to the electrical conductivity of SnO$_2$, being sensitive to the gas environment [33]. Also,
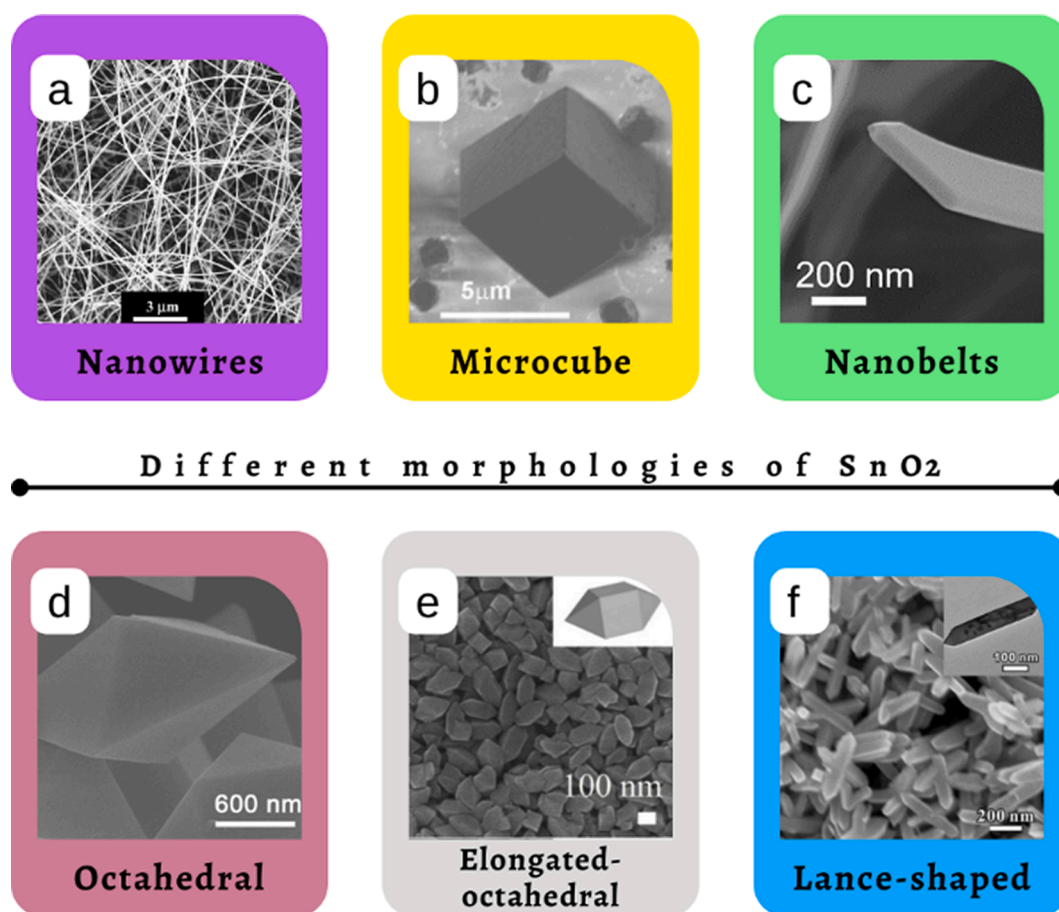

Fig. 1. Different morphologies of SnO$_2$: **(a)** nanowires [21], **(b)** microcube [22], **(c)** nanobelts [23], **(d)** octahedral [24], **(e)** elongated-octahedral [25], and **(f)** lance-shaped [26]. Reprinted from [21], Copyright 2022; [22], Copyright 2008; [23], Copyright 2021; [24], Copyright 2015; [25], Copyright 2020, with permission from Elsevier. Reprinted from [26], Copyright 2009, with permission from John Wiley and Sons.

Choi et al. investigated the gas sensor of the SnO_2 nanosheets to sense H_2 gas in terms of the variation in their resistance and, according to the results, the response of the sensor exhibited linear increase with increasing square root of the partial pressure of H_2 gas. This result indicated the applicability of the prepared sensor structure for the real field application [34]. Choi et al. also investigated the SnO_2 nanosheets with the (1 0 1) crystal face mainly exposed for selective alkene gas sensing, and it was found a remarkable selectivity to alkenes gases that can be related to the high HOMO energies [35].

Recently, Desimone et al. evaluated the power − law response and how it depends on the surface chemistry of the SnO_2 nanostructured sensors in the presence of oxygen and reducing gases. Theoretical and experimental results suggest that oxygen is adsorbed/desorbed neutral, as predicted by the Wolkenstein theory of chemisorption, and ionosorbs doubly charged [36]. The doubly charged species of ionized oxygen were also proposed by Li et al. [37]. They have proposed that the dissociation and ionization of oxygen molecules occurs when molecular oxygen are adsorbed above the in-plane oxygen vacancy vertically on SnO_2 (1 1 0) and charge transferred were both the maximum, which further verified the spontaneous adsorption of O_2 molecule and the assumption for O^- or O^{2-} species. In this case they consider the band bending presence for the applied conduction model.

On the other hand, Zhao et al. proposed a sensing model for the SnO_2-based sensors based on experimental and theoretical results to understand the effect of oxygen partial pressure on their sensitivity where the O^{2-} species was determined to be the main oxygen species [38]. Very recently, one of us analyzes the basic gas detection mechanisms proposed in such a work. The consequence of these presented mechanisms leads to inconsistencies that are also regularly found in the literature [39].

Very recently, Wang et al. published a complete review in which the preparation method of the SnO_2 nanostructure, the types of gas detected, and the improvements of their gas-sensing performances are presented as well as the future development of SnO_2 is discussed [40]. In fact, the details of the basic mechanisms that take place in sensing with metal oxides are still controversial after decades of active research in the field. There are two widely accepted models to explain the sensor behavior. In the first model, the one described above, the ionosorption model, considers that oxygen chemisorbs trapping electrons from the bulk of the grains. This alters the electronic density of the semiconductor directly affecting the film conductivity. The second model (the vacancy model) explains sensing by changes in the concentration of the surface oxygen vacancies and their ionization. Since oxygen vacancies behave electrically as donors, they would contribute to increasing the film conductivity [41].

Within the vacancy model, Blackman have recently proposed a surface conductivity model suggesting that the origin of gas sensitivity in the common *n*-type gas sensing oxides is unlikely to be ionosorbed oxygen species but is rather more likely due to the presence of a surface conductivity layer formed due to surface oxygen vacancies. This model should explain the dependency of the sensor conductance and electrical capacities on the pressure of different gases [42].

Other studies showed that the exposed surfaces and morphology play crucial role in its performance in different technological applications [43–48]. Therefore, understanding of surface characteristic is key to rationalize the action mechanism in catalysis and gas sensor [19,20,49–54]. Different theoretical studies reported the surface dependent properties of SnO_2 [55–58]. By using DFT calculation, the adsorption processes of CO on the (1 1 0), (1 0 0), (1 0 1), and (0 0 1) surfaces have been analyzed and the results showed that the (1 0 1) and (0 0 1) surface orientations gathered more electrons and then better performance for CO gas sensing [55,56,59]. The adsorption of the NO and NO_2 molecules at the SnO_2 (1 1 0), (1 0 1), and (2 2 1) surfaces were also investigated. Based on the determination of the adsorption energies and the analysis of the electron transfer, the adsorbed NO molecules in the nitrogen orientation were more stable than in the oxygen orientation

on the (1 0 1) surface and this surface showed to be the most beneficial for both NO and NO_2 gas sensing performance [56]. The application of SnO_2 as gas sense of the volatile organic compounds, such as CH_3OH and CH_3COCH_3, was investigated at the (1 1 0) and (1 0 1) surfaces and the results showed that the mechanism can be explained by direct adsorption on the surfaces. The authors also reported that due to the bipolar nature of the − OH presented on CH_3OH, the adsorption in this molecule is generally stronger than for the CH_3COCH_3 [59].

Feng et al. find a relationship between exposed surface at the morphology and the humidity sensing property of SnO_2 was investigated with an experimental and theoretical approach. The DFT results indicated that the (1 0 1) surfaces adsorbed more H_2O molecules than the (1 1 0) surfaces, in which was consistent with the experimental data. According to the authors, these results demonstrated that it is possible to improve the humidity-sensing properties of the SnO_2 semiconductor by tuning the morphology and the exposed surfaces [60].

Computational studies have been performed to provide detail information about the gas sensing action of SnO_2 on its surfaces [61–67]. Habgood and Harrison in a seminal work an ab initio study of O_2 adsorption on SnO_2 (1 1 0) surface. To this end, the authors modelled four scenarios for the placement of also four adsorbate species of oxygen on the surface and, they have hence proposed geometries and some electron distributions for those species [62]. Gurlo emphasized the key role of crystal shape on the nanosensor behavior of SnO_2, In_2O_3, ZnO, and WO_3 [65,66] and offers a description of the history of development of ionosorption theory [68]. Kucharski and Blackman reviewed the proposed models of adsorption and reaction of oxygen on SnO_2, and they conclude that the majority of evidence points to the mechanisms are center around the oxygen vacancies (V_o), being the SnO_2 surface an exchange zone between the bulk and the gas-phase oxygen. Therefore, the sensors response of the SnO_2 can be seen as resulting from the change in the position of this exchange equilibrium [63].

In addition, Barsan et al. reported the modeling of sensing and transduction for p-type semiconducting metal oxide based gas [69], while Degler et al. identified the active oxygen species in SnO_2 based gas sensing materials by an operando infrared spectroscopy [70]. Anpo et al. characterize the reactivity of oxygen species at the surface of metal oxides [71] while Salvini et al. employed the DFT calculations to investigate how the selectivity and reactivity of SnO_2 surfaces toward the CO_2 reduction revealed to formic acid change at varying surface stoichiometry (i.e., reduction degree) [72].

As we can see, SnO_2 sensing properties are directly affected by the exposed surfaces with distinct density of unsaturated Sn atoms with dangling bonds, which are results of the synthesis [63,73]. These zones are defect regions that can interact with the air or can provide extra electrons during the gas sense activities. According to DFT calculations, prior to the dissociation, the interaction of the O_2 with the unsaturated Sn atoms occurs at end-on and side-on configurations correspond to superoxide and peroxide species, respectively [61]. Yuan et al. presented a new strategy to enhancing sensing performance of SnO_2 nanocrystals by increasing the density of unsaturated Sn atoms with dangling bonds at the SnO_2 surface through hydrogenation. These authors propose a concept of the surface unsaturated Sn atoms, as active sites for the sensing and catalytic reaction mechanisms and designing advanced sensing sensors, catalysts and photoelectronic devices. Fig. 2 displays a schematic representation of SnO_2 sensing mechanism [74].

1.2. Exposed surface and morphology

The surface structure is primarily determined by the specific exposed surface. Surface energetics of materials determines their structure, properties, and occurrence of morphology. One of the rational ways of designing high-performance catalysts or gas sensors, therefore, is to engineer the exposed surface where the presence of catalytic active sites strongly enhances reactivity. Using a combination of experimental techniques and Wulff construction, we investigated the thermodynamics
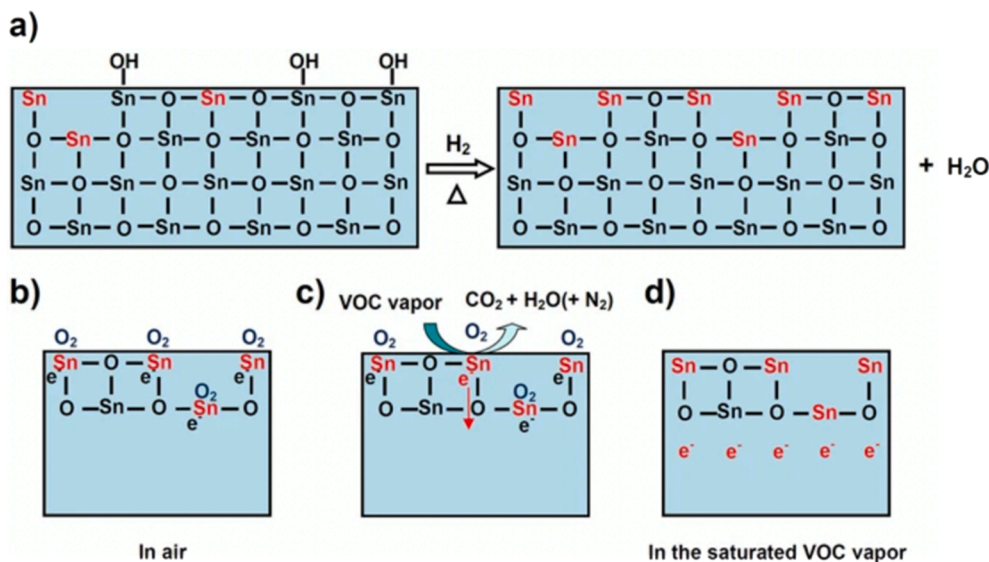
Fig. 2. Schematic diagrams of sensing mechanism. (**a**) Hydrogenation reaction of SnO_2 nanocrystals. (**b–d**) Sensing reaction mechanism of the hydrogenated SnO_2 nanocrystals at atomic and molecule level. The black e – and red e – represent the absorbed electrons by O_2 and free electrons, respectively [74]. Reprinted from [74], under the terms of the Creative Commons CC BY license.

to understand and predict the morphologies of materials [8,75–79]. It is based on the surface energy (E_{surf}), as a fundamental quantity to understand surface-related phenomena, to characterize the surface stability and can help understand the growth of crystals. Their value is dependent on the surface atomic arrangements and trap states/defects, the effective mass of hole/electrons, thus affecting the key factors such as molecule adsorption and activation, electronic band structure, and charge transfer processes [1]. More specifically, the energy and stability of the exposed surfaces are usually the primary concern, and the more stable and unstable surfaces remain and disappear along the growth process, respectively. Unfortunately, this criterion does not provide details about the morphology evolution and cannot answer why cubes can evolve into rods along the time progress of a given synthesis, for example.

It is well known that many properties of solid materials are controlled by the presence of defects and imperfections in their crystal structure. They are intrinsic or extrinsic imperfections in materials, which are not always negative and have many positive impacts on material properties. On one hand, they often display a higher reactivity proportional to the number of surface states and defects, on the other hand the same surface states and defects control the global efficiency of the process [80–82]. A comprehensive understanding of the corresponding mechanisms thus entails a description of the defective states in terms of their concentration, local structure and spatial distribution, since all of these affect the response and the chemistry that the material is able to drive [83–85]. Characterization techniques based on positron annihilation lifetime spectroscopy (PALS) is extremely powerful in defining the structural and spatial aspects of defects in materials. PALS allows to identify and quantify different types of defects and the corresponding Doppler broadening provides information not only about the defects but also on the atomic species that decorate the positrons trapping sites (i.e., chemical environments) [86].

The focus of this theoretical work is the investigation of the exposed surfaces at the morphology of the SnO_2 semiconductor to rationalize the properties and application as a multifunctional material. The aim of the present study is five-fold: (i) to assess the surface properties of low and high index surfaces of SnO_2 semiconductor using first-principles calculations, at the DFT level; (ii) to provide further detailed analysis on the relationship between the surface structures and their stabilities; (iii) to obtain the available morphologies of SnO_2 from the calculated surface energy values using the Wulff construction; (iv) to design the reaction

path along the synthesis progress to match the experimental morphologies, observed in the images of electron microscopy, with those theoretically predicted; and (v) to rationalize the growth mechanism associated to a given morphology.

2. Theoretical methods and model systems

All calculations were carried out with the Vienna *ab initio* Simulation Package (VASP) [87–90]. To determine the electron exchange and correlation contributions to the total energy, the Kohn–Sham equations were solved using the generalized gradient approximation in the Perdew–Burke–Ernzerhof functional [91,92]. The conjugate gradient energy minimization method was used to obtain the minimum (relaxed) energy state of the SnO_2. Atoms are considered fully relaxed when the Hellmann — Feynman forces converge to less than 0.005 eV $Å^{-1}$ per atom.

In this work, the low index of Miller ((001), (101), (110), (100) and (111)) surfaces and high index of Miller ((210), (102), (201), (211), (112), and (221) surfaces) have been investigated. These SnO_2 surfaces models were constructed from the data of the optimized bulk by considering stoichiometric models with thickness of up to ~20 Å. This thickness was used to reach an adequate convergence on the corresponding E_{surf} values, and then, obtain an accurate description of the surfaces. A vacuum spacing of 15 Å was introduced in the z-direction toward the surfaces so they do not interact with each other. During the optimization calculation, all atoms were allowed to relax.

A plane-wave basis set was used to describe the electron–ion interaction by the projector augmented wave method [93]. For the modeling of bulk and surfaces the plane-wave expansion was represented by 520 eV cut-off. The Brillouin zones were samples using (4 × 4 × 4) and (4 × 4 × 1) Monkhorst-Pack special k-points grid for bulk and surfaces, respectively. Previous tests have been carried out to verify that the chosen cut-off, vacuum spacing, and dimensions of Brillouin zone is sufficient, thus ensuring accurate and consistent results.

The E_{surf} values, defined as the total energy per replicating cell on the surface, were calculated for all surfaces models using the equation: $E_{surf}^i = E_{slab}^i - nE_{bulk}^{SnO_2}/2A$, where E_{surf}^i is defined as the total energy per replicating cell on the surface, E_{slab}^i is the total energy of the corresponding slab (i), n is the number of molecular units present on the slab, $E_{bulk}^{SnO_2}$ is the energy of the perfect crystal per molecular unit and 2A

corresponds to the surface area per repeating cell of the two sides of the slab. The surface broken bonds density (D_B) it was also calculated for all surfaces models by using the equation: $D_B^i = n_B/A$, where n_B is the number of broken bonds at the top of each slab (i) and A is the area of the slab. In order to know the composition of the morphology, it was also calculated the polyhedron energy ($E_{polyhedron}$) and the percentage of contribution of each surface present in the morphology. $E_{polyhedron}$ is calculated by means of: $E_{polyhedron}^i = \sum_i C_i \times E_{surf}^i$, where C_i is the percentage contribution of the surface area to the total surface area of the polyhedron $C_i = A^i/A^{polyhedron}$.

Using the values of E_{surf}^i for the all surfaces and the Wulff construction, as it was proposed by our research group [75–77], we are capable to obtain the available set of morphologies of SnO$_2$, as it is schematically illustrated in Fig. 3, in which the crystal morphology depends on the ratios between the values of the surface energies and the symmetry and crystal structure [75,94].

In addition, the calculated and available experimental morphologies were compared and matched. For other experimental observed morphologies, we present necessary modifications to the values of E_{surf} and the reaction path, through the values of $E_{polyhedron}$, along the synthesis progress are theoretically predicted. The results are expected to be helpful in choosing surface-specific interactions in synthesizing SnO$_2$ crystals with targeted morphologies.

3. Results and discussion

3.1. Bulk and surfaces

The crystallographic unit cell of SnO$_2$ is shown in Fig. 4(a). The tetragonal rutile SnO$_2$ structure is fully determined by the lattice parameters $a = b$ and c and is formed by two-unit formula per cell ($Z = 2$), belongs to $P4_2/mnm$ space group [95]. In this structure, the Sn cations have a coordination number of 6, which means that they are surrounded by an octahedron of 6O anions, while the O anions have a coordination number of 3, resulting in a trigonal planar coordination. Therefore, the tetragonal SnO$_2$ structure has the [SnO$_6$] clusters as building blocks, as illustrated on Fig. 4(a).

To investigate the exposed surfaces at the morphologies of the as-synthetized SnO$_2$ samples, low and high index of Miller were selected (see Fig. 4). As can be observed on the surfaces models showed on Fig. 4 (b, c), the surfaces presented different kinds of [SnO$_x$] clusters, i.e., the Sn atoms were coordinated by a different number of O anions, presenting breaking bonds when compared to the bulk which is formed by

[SnO$_6$] clusters. These [SnO$_x$] clusters are the places where the perfect periodic arrangement is disrupted or broken, and they can be considered as the active sites controlling the activity performance.

The top of the surface's models with low index of Miller (Fig. 4(b)) are mainly formed by [SnO$_5$] clusters and in the (1 1 1) surface is also present the [SnO$_3$] cluster, except the (0 0 1) surface model which is constituted by [SnO$_4$] clusters. On the other hand, in the surface's models with high index of Miller, all surfaces present the [SnO$_4$] and [SnO$_5$] clusters in the top of the surfaces, with exception of (2 2 1) surfaces that are only the [SnO$_5$] clusters. The surface with high index of Miller (2 1 0), (1 0 2), (2 0 1), (2 1 1), (1 1 2), and (2 2 1) as can be seen in the Fig. 4(c), where these models presented antisymmetric surfaces.

From the results of the slab models' calculations, E_{surf} and D_B values were obtained for all surfaces; they are listed in Table 1.

As can be observed, the stability order of the low index surfaces is: (1 1 0) < (1 0 0) < (1 0 1) < (0 0 1) < (1 1 1), while for the high index is: (2 0 1) < (2 1 1) < (2 2 1) < (2 1 0) < (1 0 2) < (1 1 2). In the set of all surfaces, there are surfaces with high index of Miller that are more stable than some surfaces with low index of Miller. Therefore, the stability order for all calculated surfaces is: (1 1 0) < (1 0 0) < (2 0 1) < (2 1 1) < (1 0 1) < (2 2 1) < (2 1 0) < (0 0 1) < (1 1 1) < (1 0 2) < (1 1 2). Some theoretical investigations have been discussed about the stability of the SnO$_2$ surfaces applying different functionals (see Table 2). By employing the B3LYP functional, our research group obtained the following stability order (1 1 0) < (1 0 0) < (1 0 1) < (2 0 1) < (0 0 1) [51]. Using the DFT with the generalized gradient approximation (GGA), the E_{surf}, calculated by Oviedo and Gillan, increased in the order (1 1 0) < (1 0 0) < (1 0 1) < (0 0 1) [96]. Mulheran and Harding using the local-density approximation (LDA) obtained the following surface stability: (1 1 0) < (2 1 0) < (1 0 1) < (1 0 0) < (3 1 0) < (3 2 1) < (2 1 1) < (3 0 1) < (1 1 1) < (0 0 1) [97]. Also using the LDA, Slater et. al. reported the E_{surf} value order as (1 1 0) < (2 1 0) < (1 0 1) < (1 0 0) < (3 1 0) < (3 2 1) < (2 1 1) < (3 0 1) < (3 1 1) < (1 1 1) < (0 0 1) < (2 1 2) < (2 2 1) < (1 1 2) [98]. In Fig. 5 a schematic representation of the values for energy surfaces calculated with different functionals is depicted. An analysis of the results renders that LDA gives higher values than B3LYP and GGA for the low index of Miller surfaces: (0 0 1), (1 0 1), (1 1 0), (1 0 0).

As can be observed in the Table 1, the order of the D_B values are not completely consistent with the stability order for all calculated surfaces. This is due to the existence of dangling Sn–O bonds in the exposed surfaces and, as a consequence, the presence of incomplete octahedral [SnO$_6$] clusters, as can see in Fig. 4(b,c). The morphology of SnO$_2$ with surface unsaturated Sn cations (clusters) serve as signature of the surface stability, which could be responsible for the properties and growth
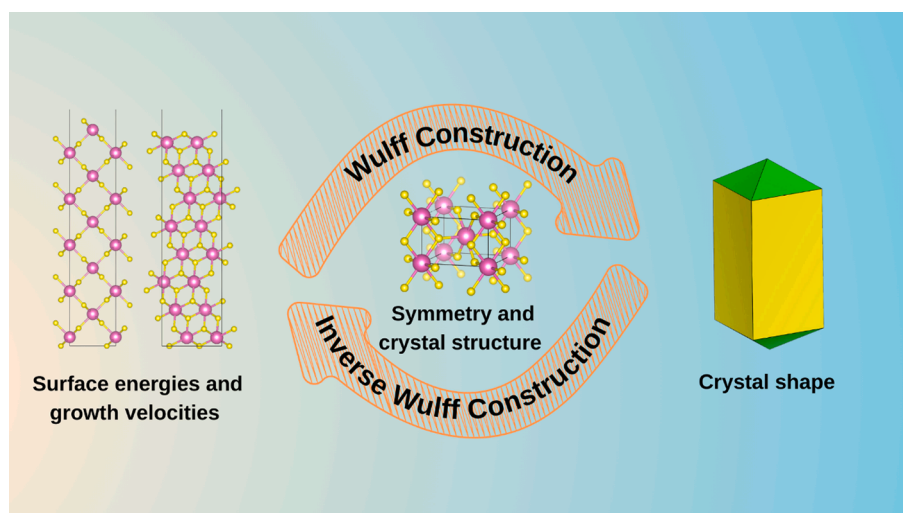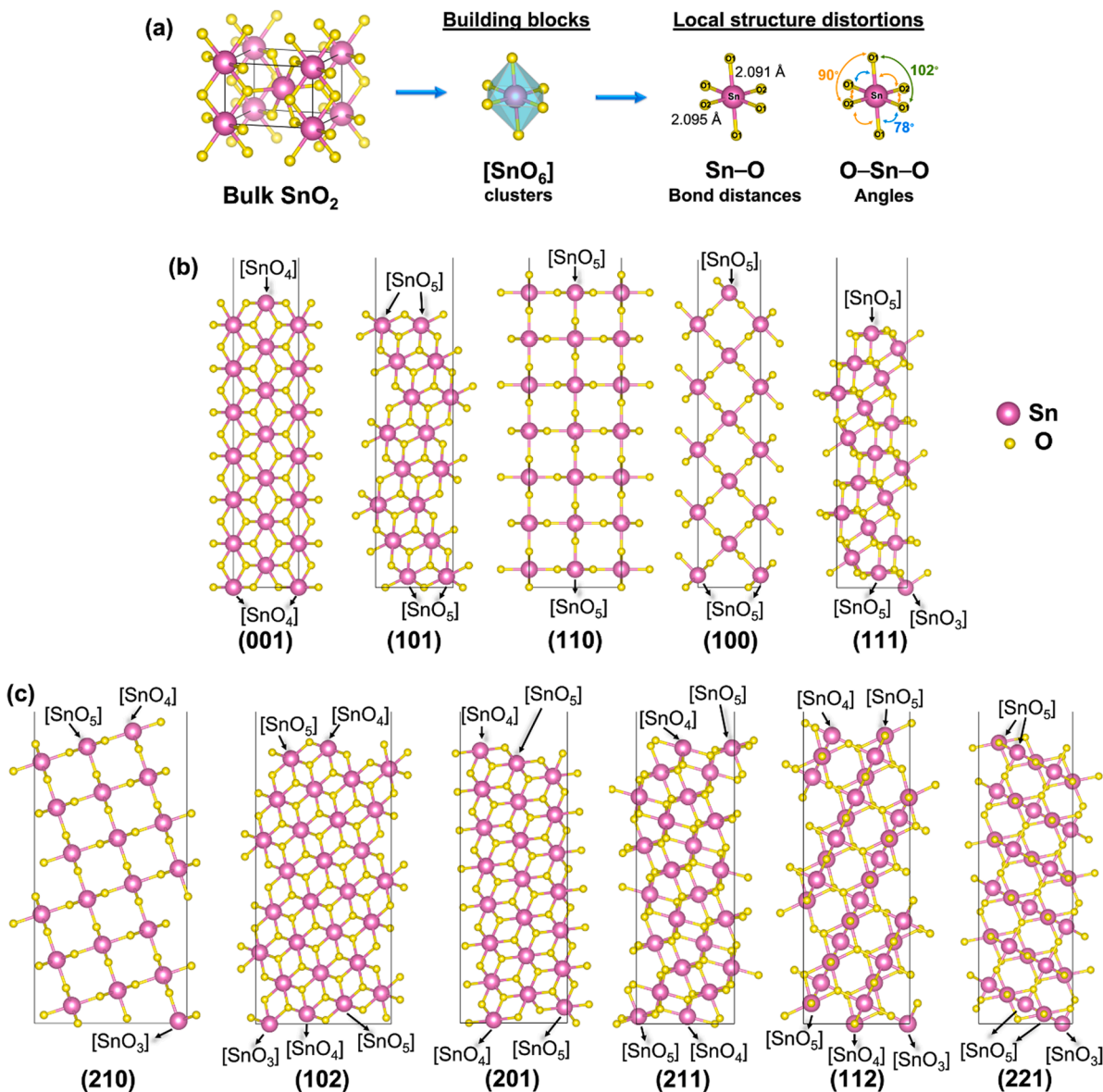

Fig. 3. Illustration of the step for the modeling of crystal morphology by applying the forward and inverse Wulff construction.

Fig. 4. (a) The unit cell of the tetragonal SnO_2 structure, with the $[SnO_6]$ clusters, bond distances and angles between the Sn and O atoms. (b) The low index of Miller surfaces: (001), (101), (110), (100), and (111). (c) The high index of Miller surfaces: (210), (102), (201), (211), (112), and (221).

Table 1
Surface energy values ($E_{surf}, J/m^2$) and surface broken bonds density (D_B, nm^{-2}) for all investigated SnO_2 surfaces.

Low index	E_{surf}	D_B	High index	E_{surf}	D_B
(001)	1.84	8.57	(210)	1.60	11.43
(101)	1.44	10.68	(102)	2.05	8.13
(110)	1.00	9.03	(201)	1.42	10.24
(100)	1.08	6.39	(211)	1.43	7.13
(111)	1.97	3.11	(112)	2.15	5.81
			(221)	1.59	4.00

crystal mechanism. More importantly, these defects could induce extra electronic energy levels above the top of the valence band (VB) or below the bottom of the conduction band (CB), generating new intermediate energy levels in the prohibited zone (band gap). These discrete levels are the key for the multifunctional properties and applications of semi-conductors. Along the photocatalytic process, they act as trapping centers of the CB for releasing electrons in the excited state and in the VB for trapping electrons for the photogenerated charge carriers, resulting in the effective variation of the charge density at the surface of the semi-conductor. As a result, the highest photocatalytic activity is achieved.

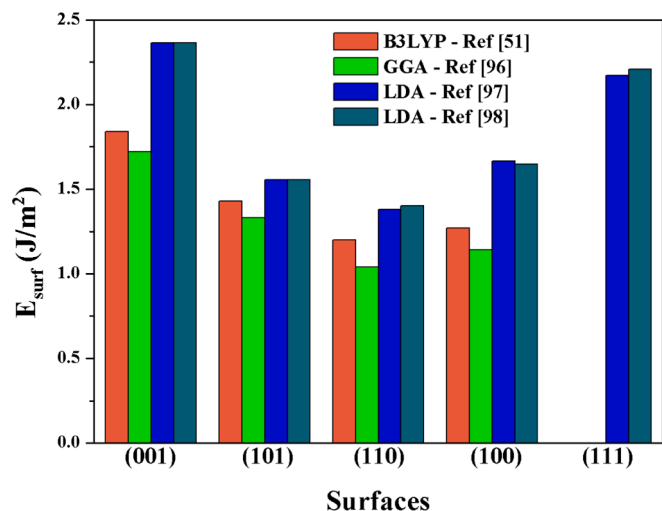At this point, it is possible to emphasize the importance of the study

Table 2
Surface energy value (J/m^2) for a set of surfaces reported by several published papers.

(001)	(101)	(110)	(100)	(111)	(112)	(201)	(210)	(211)	(212)	(221)	(310)	(301)	(321)	(311)	Functional	Ref.
1.84	1.43	1.20	1.27	–	–	1.63	–	–	–	–	–	–	–	–	B3LYP	[51]
1.72	1.33	1.04	1.14	–	–	–	–	–	–	–	–	–	–	–	GGA	[96]
2.366	1.554	1.380	1.664	2.217	–	–	1.487	1.821	–	–	1.679	1.860	1.758	–	LDA	[97]
2.363	1.554	1.401	1.648	2.209	3.677		1.480	2.135	2.351	2.280	1.973	1.824	1.731	2.051	LDA	[98]

Fig. 5. A comparative diagram depicting the values of surface energy calculated by different levels of theory for the low index of Miller surfaces: (0 0 1), (1 0 1), (1 1 0), (1 0 0), and (1 1 1).

not only of the surfaces and the morphologies of a given semiconductor, but also the arrangement of the atoms on the exposed crystal shape. In the case of SnO_2, these atoms constitute clusters with vacancies, which we will name V_o. In this way, it is possible to write the clusters present at the surfaces as a function of the number of V_o using the Kröger-Vink

notation, as can be seen in Fig. 6. The Sn cations at the surfaces can be also called as Sn_{5c}, Sn_{4c}, and Sn_{3c} according to the number of V_o (one, two, or three, respectively) in the undercoordinated Sn clusters.

From this analysis, the defect regions of the material at the surfaces can be described with undercoordinated clusters having oxygen vacancies as $[SnO_x \bullet 6-xV_o]$, where x represents the V_o numbers ($x = 3$, 4 or 5). These vacancies can have two paired electrons (high electron density, HED), no paired electrons (low electron density, LED) or one electron in the excited state (EES) with alpha or beta spin. Therefore, there is the probability of transferring an electron from HED to LED or EES.

3.2. Positron annihilation lifetime spectroscopy

PALS, utilizing positron–electron pair annihilation, is a powerful technique for the probing and characterization of the electronic and atomic structures at polar regions in condensed matter, such as point-defects, voids, interfaces and surfaces, among others, providing information about their size, concentration, and chemical environment [99]. The advantages of the use of PALS to study defects lie in the fact that positrons are prone to be localized and annihilated in sites with greater electronic density (i.e., more negative) than the average electronic density of the crystal lattice, allowing positron annihilation processes to take place in these sites, which act as positron traps with an associated specific open volume. Analysis of the PALS results have demonstrated to be a powerful tool to investigate the presence of vacancy-like defects in semiconductors [100]. From the positron lifetime spectra decomposition, several lifetime components can be extracted; each of them is
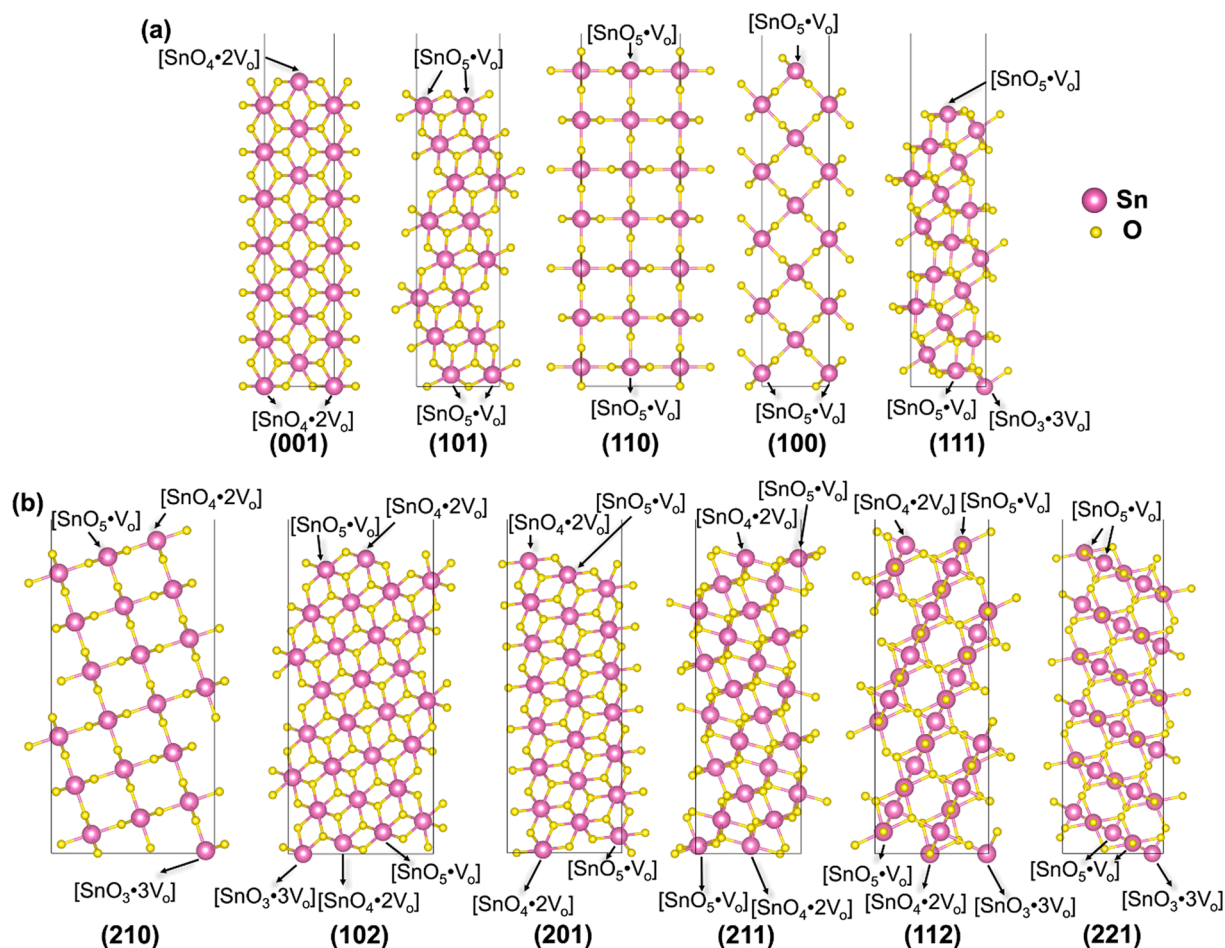

Fig. 6. Surfaces models with the Kröger-Vink notation for the **(b)** low index of Miller surfaces: (0 0 1), (1 0 1), (1 1 0), (1 0 0), and (1 1 1), and for the **(c)** high index of Miller surfaces: (2 1 0), (1 0 2), (2 0 1), (2 1 1), (1 1 2), and (2 2 1).

characterized by a lifetime τ_i and an associated intensity I_i. The state i can be the delocalized one in the crystal lattice (free positron state) or localized states at different defect sites where positrons become trapped and annihilated. The presence of more than one lifetime indicates that the studied sample is not defect-free, which is common in semiconductor oxide samples.

There are several published papers that used this technique to investigate the defects in different semiconductors such as silica glass [101], β-Cu-Zn-Al alloys [102], BaTiO$_3$ [103], UO$_x$ (x = 2.2–3.5 range) [104], ZnO-based varistors [105], α-Ag$_2$WO$_4$ [106], among others [107–110]. In the case of SnO$_2$ semiconductors, Macchi et al. reported the characteristics of vacancy-like defects in nanocrystalline commercial high-purity powders and the influence of the annealing treatment under different atmospheres by applying the PALS analysis [110]. According to the authors, it was detected in all samples two types of vacancy-like defects: i) vacancy clusters formed by Sn and O vacancies (at the surface of the grains), and ii) Sn-based vacancies associated with small open volumes (typically, mono- or di-vacancies inside the grains).

At this point, it is important to remark that deepening of future experimental studies will lead to elucidate, for each exposed crystalline plane, the corresponding conduction mechanisms that explain the variation in electrical resistance when exposed to different gaseous atmospheres.

3.3. Theoretical morphologies

From the E_{surf} values and the association to the Wulff construction some morphologies for the SnO$_2$ with the low Miller indices were obtained, as illustrated in Fig. 7.

Considering the theoretical calculations with low index of Miller and using the Wulff construction, the equilibrium morphology was achieved (in the center of the Fig. 7) and this result suggests that the (101), (110) and (100) surfaces are predominated and correspond to 36.4%, 40.7%, and 22.9%, respectively. To obtain the others morphologies present in Fig. 7, the E_{surf} value of the equilibrium morphology in a determinate surface direction was decreased, which means a stabilization of this surface. The stabilization/destabilization of the surface simulates the process that can occur during the syntheses of the semiconductor and the change in the final morphology and, consequently, in the exposed area.

In the case of the SnO$_2$, it was seen that some surfaces with high index of Miller present a higher stability in respect to the low index of Miller. Therefore, it was constructed a map of morphologies with the present of all calculated surfaces, as illustrated in Fig. 8.

In the Fig. 8, the equilibrium morphology (a) is presented in the center of the figure. This crystal is formed by low and high index of Miller and is formed by the (101), (110), (100), (201), and (211) surfaces. Here, with the presence of the high-index surfaces, there is a decrease in the area of the (101), (110), and (100) surfaces to 29.3%, 37.7%, and 21.5%, respectively, with 4.3% and 7.1% for the (201) and (211) surfaces, respectively. Nonetheless, the three low index (101), (110), (100) surfaces are still dominating in the Wulff shape and make up almost 88.6% of the total crystal surface area. The E_{surf} values with each percentage contribution for each morphology from Fig. 8 are listed in Table 3.

The morphologies presented in Fig. 8 were obtained also by decreasing the E_{surf} value towards all surfaces, where the orange and blue arrows mean that this decrease is in direction of the low and high index of Miller, respectively. The orange arrows give origin to the first circle of morphologies in the map. The stability of the (110), (101),
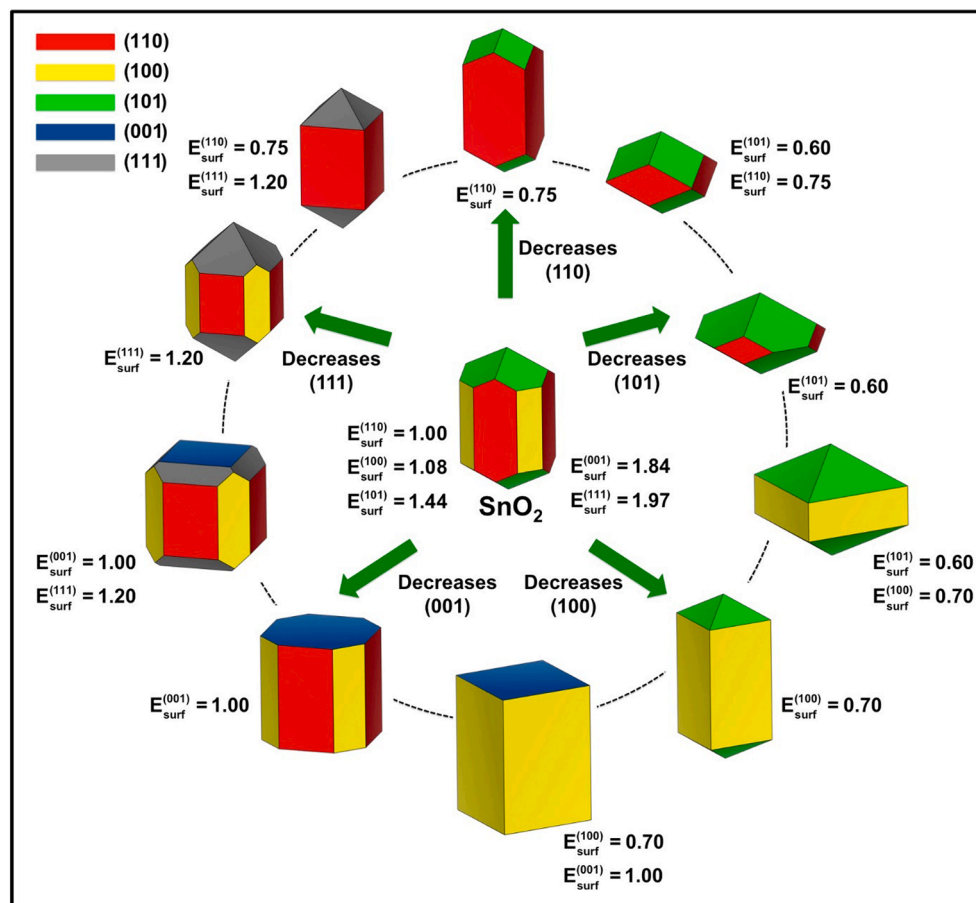

Fig. 7. Map of morphologies for the tetragonal SnO$_2$ structure with the low index of Miller surfaces: (001), (101), (110), (100), and (111). E_{surf} in J/m^2.
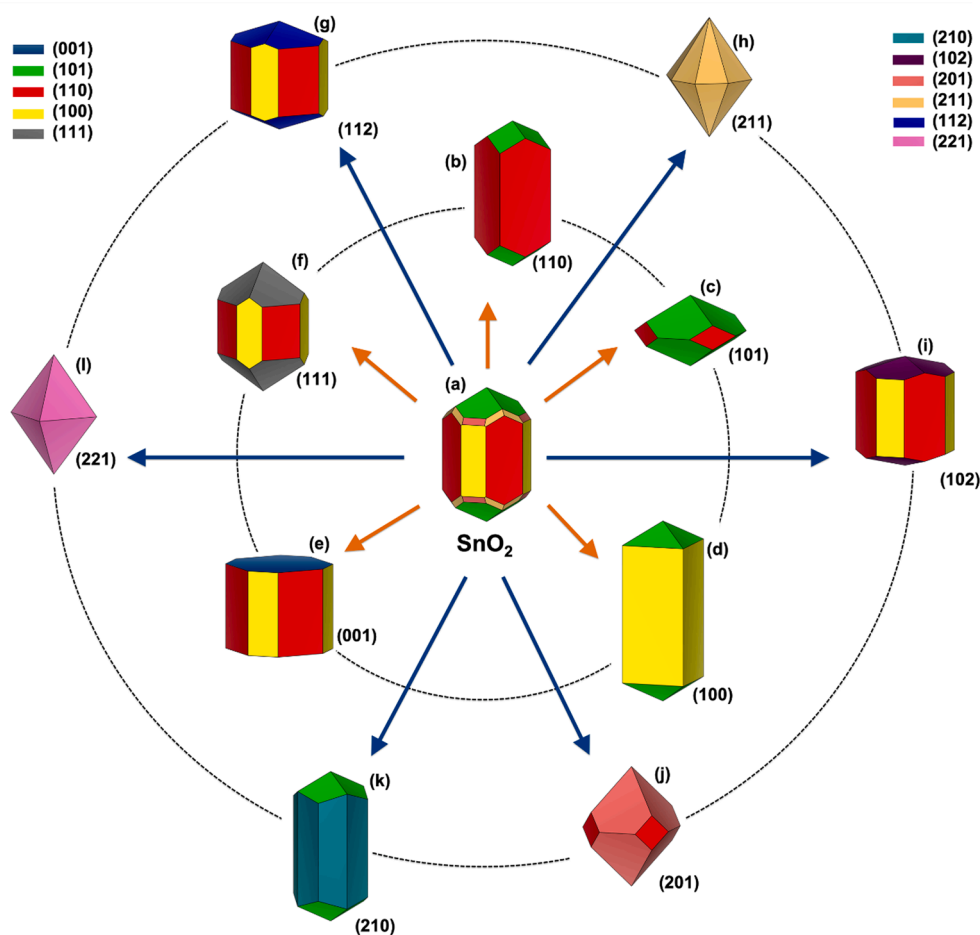
Fig. 8. Map of morphologies for the tetragonal SnO_2 structure with the low index of Miller: (001), (101), (110), (100), and (111) surfaces and with the high index of Miller: (210), (102), (201), (211), (112), and (221) surfaces.

Table 3
Surfaces with its surface energy value (E_{surf}, J/m^2) and its percentage of contribution for the morphology (in parentheses, %).

Crystal shape
Surface = E_{surf} (contribution)

(a)	(d)	(g)	(j)
$(101) = 1.44$ (29.3)	$(101) = 1.44$ (21.7)	$(110) = 1.00$ (35.2)	$(110) = 1.00$ (10.4)
$(110) = 1.00$ (37.7)	$(100) = 0.61$ (78.3)	$(100) = 1.08$ (23.8)	$(201) = 0.80$ (89.6)
$(100) = 1.08$ (21.5)		$(112) = 1.15$ (41.0)	
$(201) = 1.42$ (4.3)			
$(211) = 1.43$ (7.1)			
(b)	**(e)**	**(h)**	**(k)**
$(101) = 1.44$ (24.3)	$(001) = 0.90$ (36.4)	$(211) = 0.78$ (100.0)	$(101) = 1.44$ (28.1)
$(110) = 0.67$ (75.7)	$(110) = 1.00$ (38.9)		$(210) = 0.80$ (71.9)
	$(100) = 1.08$ (24.7)		
(c)	**(f)**	**(i)**	**(l)**
$(101) = 0.60$ (89.2)	$(110) = 1.00$ (29.0)	$(110) = 1.00$ (39.8)	$(221) = 0.67$ (100.0)
$(110) = 1.00$ (10.8)	$(100) = 1.08$ (21.4)	$(100) = 1.08$ (23.6)	
	$(111) = 1.18$ (49.6)	$(102) = 1.20$ (36.6)	

(100), (001), and (111) surfaces formed the morphologies (b), (c), (d), (e), and (f), respectively. How it is possible to observe, these morphologies are also presented in the Fig. 7. The second circle of morphology (blue arrow direction) are constituted by the (112), (211), (102), (201), (210), and (221) surfaces which originate the morphologies (g), (h), (i), (j), (k), and (l), respectively. As we can see in Fig. 8 and Table 3, the most stable (110) surface is present in 66.7% of the morphologies, in which the responsibility for the properties of the semiconductor is assigned.

3.4. The way to morphology-controlled synthesis: How far do we need to go?

One of the recent trends in semiconductors investigation is the control of material morphology due to the significant effect on their electronic, (photo)catalytic, and electrical properties. The final morphology of material is governed by the preferred growth regime of the synthesis reaction process. The first important aspect is the choice of the method of synthesis, following by several critical parameters such as type and concentration of the reactants, the kind of the solvent, time, and pressure of the reaction, and also the applying of surfactants. Therefore, the final morphology will be composed by different exposed surfaces, resulting in several shapes with difference electronic density. These aspects are summarized in Fig. 9.

A wide range of morphology-controlled synthesis of SnO_2-based materials have been reported in the literature under different reaction conditions. Shen and co-authors investigated the influence of the SnO_2 morphologies on the H_2 sensing properties. They fabricated the SnO_2 as
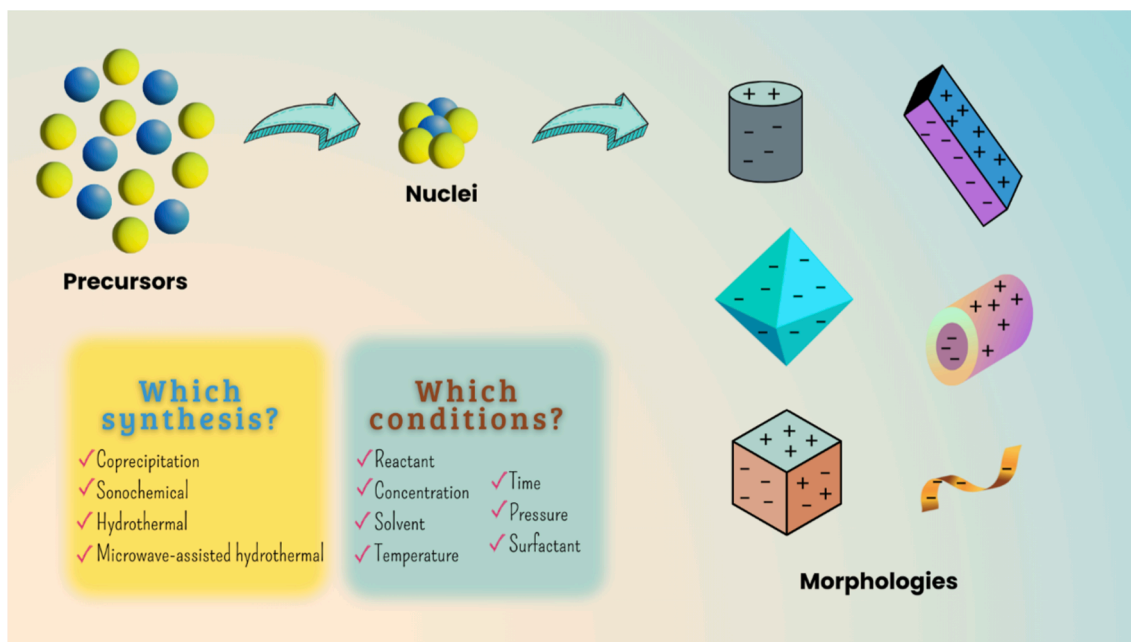
Fig. 9. Schematic illustration for the factors that influence in the final morphology.

nanofilms by the sputtering methods and nanorods and nanowires by the thermal evaporation method, showing that the morphology and structure of semiconductor materials plays in determining its gas-sensing properties [111]. Xu and co-authors synthetized an ultrathin SnO_2 nanosheets with dominant high-energy (0 0 1) surface for low temperature formaldehyde (HCHO) gas sensor [112]. The ultrathin SnO_2 nanosheets were obtained by a facile hydrothermal method with the assistance of any template, surfactant, or organic solvent. According to the authors, the good performance of the ultrathin SnO_2 nanosheets as HCHO gas sensor is due to the high percentage of the (0 0 1) surface with the undercoordinated atoms on the surface which improved the catalytic activity of the surface atoms [112].

The tetragonal rutile structure of SnO_2 were synthetized by a simple hydrothermal route by Xing and co-authors [113]. The SnO_2 nanoparticles were tested for enhanced photocatalytic activities and the results of degradation of several kinds of organic dye molecules showed that eosin red solution is almost completely degraded after 18 min under ultraviolet light irradiation. The study of cyclic stability results demonstrated that the SnO_2 nanoparticles possess still excellent photocatalytic activity after 5 times cycles, revealing its potential applications in eliminating the organic contaminants in wastewater. According to the authors, the SnO_2 nanoparticles are constituted by the (1 1 0) surfaces.

The effect of different morphologies of the SnO_2 nanostructured on its photocatalytic activities were investigated by Kar et al. According to the authors, the modulation of the morphology changes the surface area and levels of surface defects in which reflected in the photocatalytic degradation of the methylene blue dye [114].

3.4.1. Reaction path along the synthesis progress and the polyhedron energy

SnO_2 particles with different shapes (octahedral, elongated-octahedral and lance-shape) were obtained by Han and co-authors [26] in a hydrothermal route at 200 °C for 12 h in an appropriate acidic environment (with hydrochloric acid, HCL, and poly(vinyl pyrrolidone, PVP). Theses morphologies are mainly formed by the high-index (2 2 1) surfaces which enhanced the SnO_2 gas-sensing properties, and this morphological change was controlled by changing the amount of HCl. From the E_{surf} values for all investigated SnO_2 surfaces (see Table 1), we were able to design a possible reaction path along the synthesis progress to match the theoretical and experimental morphologies. To this end, it was calculated the $E_{polyhedron}$ for the octahedral (1b),

elongated-octahedral (2b) and lance-shape (3b), passing through the 1a, 2a and 3a, respectively, from the equilibrium morphology, as illustrated in Fig. 10. According to the authors, the SnO_2 octahedral (1b) exhibit far better gas-sensing performance over ethanol than those morphologies that mainly have the (1 1 0) exposed surfaces, and, from the theoretical point of view, this morphology also present higher $E_{polyhedron}$ value. Therefore, these results shown that the gas-sensing is facet-dependent according to the exposed surfaces and atomic arrangement.

3.4.2. Growth mechanism to modulate the surface termination of SnO_2-based materials

The crystal growth mechanism is an important issue mainly due to the interest in controlling particle size and morphology. It is possible to predict the particle growth mechanism by using the degree of solubility and the particle size by the Ostwald − Freundlich equation or, in a colloidal system at room temperature, the grain − rotation − induced grain coalescence mechanism can be applied [52]. On the other hand, the
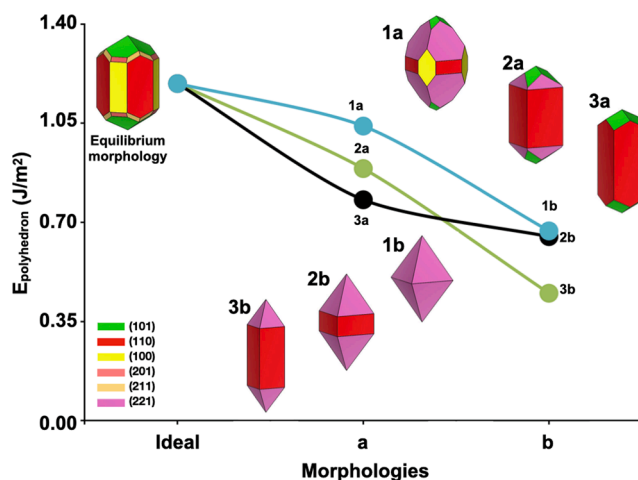

Fig. 10. Polyhedron energy value and the reaction path along the synthesis progress to obtain the experimental morphologies: octahedral (**1b**), elongated-octahedral (**2b**) and lance-shape (**3b**), passing through the **1a**, **2a** and **3a**, respectively, from the equilibrium morphology,

well-known Wulff construction provides a convenient method to evaluate the formation of macroscopic facets B of orientation $(h_2k_2l_2)$ on a surface A of orientation $(h_1k_1l_1)$. The relative energy (ΔE) can be calculated by the following expression: $\Delta E = E_{surf}^A(h_1k_1l_1)cos\theta - E_{surf}^B(h_2k_2l_2)$ where E_{surf}^A is the surface energy (per unit area) of the surface A (in the $(h_1k_1l_1)$ orientation), E_{surf}^B is the surface energy (per unit area) of the surface A (in the $(h_2k_2l_2)$ orientation), θ is the angle between the planes and the factor $cos\theta$ takes into account the change in the surface area if the facets were formed [51]. According to this expression, if ΔE it is negative, the surface B can grow stably on surface A. Using this approach and associating with previous experimental results, our research group modelized the preferential growth directions of the SnO$_2$ nanobelts, as illustrated in Fig. 11 [51]. We also performed an ex-situ observation of the orientated attachment crystal growth process of SnO$_2$ nanocrystals at room temperature using the high-resolution transmission electron microscopy [52]. Cheng et al. also explained the SnO$_2$ nanorods growth by combining the theoretical results of the E_{surf} values with the transmission electron microscope image [115].

Using this strategy, it was calculated the formation energy of all the possible facets B on all surfaces A presented in the map of available morphologies of SnO$_2$ depicted in Fig. 8 and the values is presented in the Table 4.

As it is possible to observed in the Table 4, the formation of a stable facet depends on the growth direction. For example, if the growth direction is [101] for the morphology (b), the formation of the plane (110) on the (101) is more stable ($\Delta E = -1.65$) than if is change the direction for [110], where the formation of the plane (101) on the (110) is less stable ($\Delta E = -0.09$). If we go to the morphology (c), where is formed by the same surfaces ((101) and (110)) but with different E_{surf} values, the formation of the plane (110) on the (101) continues stable ($\Delta E = -1.41$). However, for the growth direction [110], the formation of the plane (101) on the (110) is unstable ($\Delta E = 1.08$). As it is possible to see, the angle between the planes does not change and only the change in the surface values, i.e., the stabilization of a surface, alters the growth direction of the morphology by changing the formation energy.

This strategy, based on first-principles calculations, allowed us to understand and interpret, at the atomic level, the effects of morphology

control on the synthesis of semiconductors. Fine-tuning of the desired morphologies can be achieved by controlling the values of the surface energies, which leads to the formation of morphologies that the classic growth process does not allow [116–118]. In particular, we reported a detailed characterization of an anomalous oriented attachment behavior for SnO$_2$ nanocrystals [119]. In addition, this procedure is a useful approach for faceted nanocrystal shape modeling and indirect quantitative evaluation of dopant spatial distribution, which are difficult to evaluate by other techniques [58,120]. In this context, we describe a simple approach to control the oriented attachment process through selective ligand scavenging from the (100) facets of CeO$_2$ nanoclusters with desired sizes and shapes [121]. This methodology for the synthesis of CeO$_2$ may be relevant for the investigation of self-assembly processes of other metal oxides as well as for other types of inorganic nanoparticles, which brings new insight for nanostructure design and controlled synthesis [122–128].

Toku et al. proposed a new crystal plane control technique to obtain of single crystal SnO$_2$ nanobelts by thermal sublimation. The authors observed that the grow direction was different by synthesis pressure: 10 kPa or less results in the growth direction to [301], changing to [101] over 20 kPa (see Fig. 12) [23]. As can we have seen in the results of Table 4, the change in the growth direction is directly related to the E_{surf} stabilization.

Recently, Masuda have investigated the facet-controlled growth mechanism of SnO$_2$ (101) nanosheet assembled film via cold crystallization for devices such as chemical sensors. Their TEM results revealed that the predominate branch angles between any two connected nanosheets were 90° and 46.48°, corresponding to type I and type II connections, respectively. These connections were consistent with our calculations reported in Table 4, involving the combination of (001) and (110), and (111) and (110) surfaces, respectively [129].

Awareness is growing that the reactivity of materials is determined by surface properties. Therefore, processing materials with high performance requires enhanced knowledge on these properties. In addition, we need to recognize that there is a need to develop surface-processing procedures that allow modifications of surface reactivity in a controlled manner to achieve desired performance. To this end, surface characterization at the conditions of processing is required, as well as
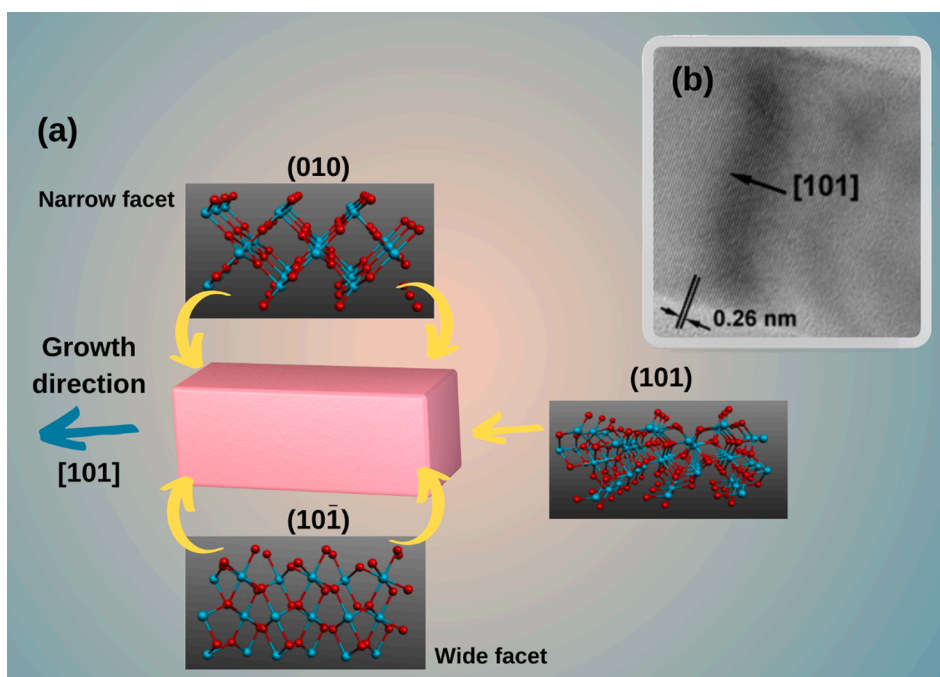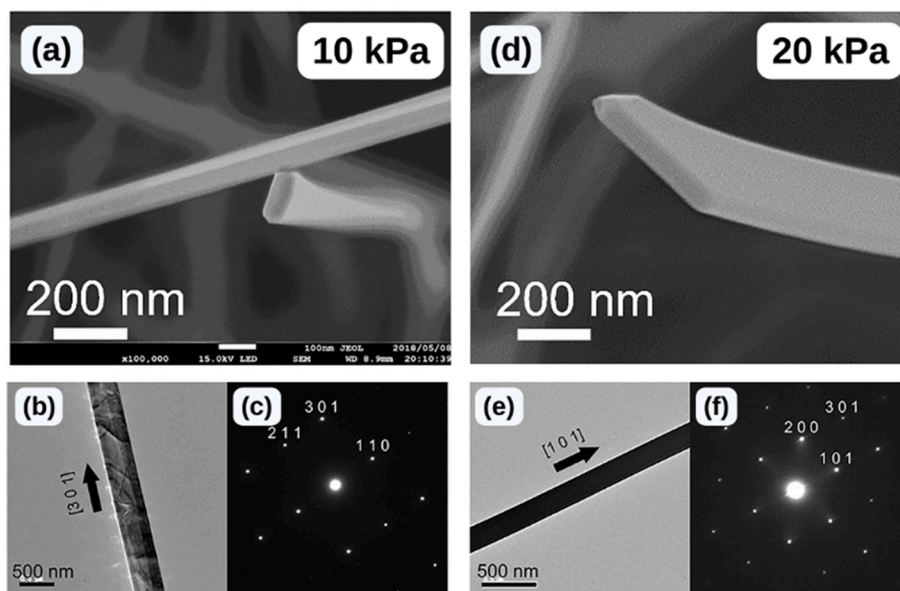

Fig. 11. (a) Proposed growth mechanism for the SnO$_2$ nanobelts and **(b)** high-resolution transmission electron microscope image [51]. Reprinted from [51], Copyright 2003, with permission from AIP Publishing.

Table 4

Calculated values of formation energy (ΔE) of the facet B on the surface A (J/m²), and angle (θ, degree) between the planes A and B for all crystal shapes reported on Fig. 6.

A\B							
(a)	(a)	(c)	(c)	(f)	(f)	(i)	(i)
(101)\(201)	(201)\(101)	(101)\(110)	(110)\(101)	(111)\(110)	(110)\(111)	(102)\(100)	(100)\(102)
19.45°	19.45°	66.80°	66.80°	46.50°	46.50°	71.46°	71.46°
ΔE = − 0.23	ΔE = − 0.85	ΔE = − 1.41	ΔE = 1.08	ΔE = − 1.96	ΔE = 0.63	ΔE = − 1.91	ΔE = 0.58
(101)\(211)	(211)\(101)	(d)	(d)	(111)\(100)	(100)\(111)	(102)\(110)	(110)\(102)
28.93°	28.93°	(101)\(100)	(100)\(101)	60.88°	60.88°	77.00°	77.00°
ΔE = − 2.57	ΔE = 0.78	56.14°	56.14°	ΔE = − 1.52	ΔE = 0.28	ΔE = − 1.04	ΔE = − 0.17
		ΔE = 0.71	ΔE = − 1.75				
(201)\(100)	(100)\(201)	(e)	(e)	(110)\(100)	(100)\(110)	(110)\(100)	(100)\(110)
36.69°	36.69°	(001)\(100)	(100)\(001)	45.00°	45.00°	45.00°	45.00°
ΔE = − 0.32	ΔE = − 0.88	90.00°	90.00°	ΔE = − 0.46	ΔE = − 0.63	ΔE = − 0.55	ΔE = − 0.45
		ΔE = − 1.48	ΔE = 0.63				
(211)\(110)	(110)\(211)	(001)\(110)	(110)\(001)	(g)	(g)	(j)	(j)
37.87°	37.87°	90.00°	90.00°	(112)\(100)	(100)\(112)	(110)\(201)	(201)\(110)
ΔE = 0.41	ΔE = − 1.42	ΔE = − 1.40	ΔE = 0.55	72.36°	72.36°	55.46°	55.46°
				ΔE = − 2.22	ΔE = 0.92	ΔE = − 0.34	ΔE = − 0.66
(100)\(110)	(110)\(100)	(100)\(110)	(110)\(100)	(112)\(110)	(110)\(112)	(k)	(k)
45.00°	45.00°	45.00°	45.00°	64.62°	64.62°	(101)\(210)	(210)\(101)
ΔE = − 0.43	ΔE = − 0.61	ΔE = − 0.43	ΔE = − 0.61	ΔE = − 1.25	ΔE = 0.07	60.11°	60.11°
						ΔE = − 2.11	ΔE = 0.27
(b)	(b)			(110)\(100)	(100)\(110)		
(101)\(110)	(110)\(101)			45°	45°		
66.80°	66.80°			ΔE = − 0.55	ΔE = − 0.45		
ΔE = − 1.65	ΔE = − 0.09						

Fig. 12. Scanning electron microscope (a and d) and transmission electron microscope (b, c and e, f) imagens of the SnO₂ nanobelts at 10 kPa and 20 kPa, respectively [23]. Reprinted from [23], Copyright 2021, with permission from Elsevier.

assessment of the effect of surface properties on reactivity and the related charge transfer. This knowledge of surface properties and the procedures for modification of surface reactivity constitutes a step forward in the development of novel advanced materials.

Overall, this study demonstrates the great potential of the present strategy for understanding the morphology evolution of SnO_2 and its transformations under reaction conditions. New insights into this complex material will be instrumental by including specific interaction with hydroxyl groups, H_2O, CO_2, CO, or some other molecules in the environment. This can reveal the mechanisms behind its excellent activity and will thus enable new pathways for the rational design of the next generation of gas sensors.

4. Conclusions

The surface of a material plays a crucial role as an interface to the environment, to control the physical, chemical, and biological properties. As such, changes of the surfaces at the morphology of a material offers a practical method of modulating the surface properties and applications. Here, we investigated the structure and stability of low and high index surfaces of SnO_2 with stoichiometric slab models with DFT calculations associated to the PBE functional. The atomic coordination environment of surface atoms was described by the undercoordinated clusters (dangling bonds), by using the Kröger-Vink notation, at the exposed surfaces with different geometry and surface broken bonds density distributions.

The main conclusions of the present work can be summarized as follows: (i) based on the Wulff construction, by modifications of the

values of E_{surf} of the different exposed surfaces, we were capable to predict the crystal morphology and to construct the complete map of available morphologies of SnO_2 by investigating the surface stability of the (001), (101), (110), (100), (111), (210), (102), (201), (211), (112), and (221) surfaces; (ii) by comparing the simulated morphologies from present models with available experimental images of field emission microscopy, we can match them quite well; (iii) for other experimental observed morphologies, we present necessary modifications to the E_{surf} values and the reaction path, through the values of $E_{polyhedron}$, along the synthesis progress are theoretically predicted; (iv) our findings explain how the values of the energy surfaces regulate the growth, evolution, and final morphology. This morphological progress provides guidelines to improve both of chemical activity and structure stability. In addition, the growth mechanism of the SnO_2 semiconductor is modulated by the stability of its surfaces, which is directly affected by the synthesis method; (v) the results are expected to be helpful in choosing surface-specific interactions in synthesizing SnO_2 crystals with targeted morphologies by adjusting surface energies contributions; (vi) our investigation helps to tune the conditions to obtain the desired morphology and can be extended to other complex oxides. Through the synergistic roles of different reaction conditions, such as the presence of surfactants, type of solvent, temperature, pressure, and so on, leading to a challenging synthesis process; and (vii) the present findings provide a new insight into the surface-dependent property, which would inspire the crystal surface tailoring and control of more semiconductors to expand their applications. Therefore, extending the method of controlled synthesis of other semiconductors into general laboratories should not take much longer.

CRediT authorship contribution statement

Amanda F. Gouveia: Conceptualization, Software, Methodology, Validation, Formal analysis, Investigation, Resources, Data curation, Writing – original draft, Visualization. **Celso M. Aldao:** Writing – review & editing. **Miguel A. Ponce:** Writing – review & editing, Supervision. **Edson R. Leite:** Validation, Supervision, Project administration, Funding acquisition. **Elson Longo:** Investigation, Writing – review & editing, Project administration, Funding acquisition. **Juan Andrés:** Conceptualization, Methodology, Validation, Investigation, Writing – review & editing, Supervision, Project administration, Funding acquisition.

Declaration of Competing Interest

The authors declare that they have no known competing financial interests or personal relationships that could have appeared to influence the work reported in this paper.

Data availability

Data will be made available on request.

Data availability

Data will be made available on request.

References

[1] W.G. Tu, W.L. Guo, J.Q. Hu, H.C. He, H.J. Li, Z.S. Li, W.J. Luo, Y. Zhou, Z.G. Zou, State-of-the-art advancements of crystal facet-exposed photocatalysts beyond TiO2: design and dependent performance for solar energy conversion and environment applications, Mater. Today 33 (2020) 75–86.

[2] X.M. Cheng, J. Zhao, W.Y. Sun, Facet-engineering of materials for photocatalytic application: status and future Prospects, Energychem 4 (2022).

[3] S. Bai, L.L. Wang, Z.Q. Li, Y.J. Xiong, Facet-engineered surface and interface design of photocatalytic materials, Adv. Sci. 4 (2017) 1600216.

[4] R.G. Li, F.X. Zhang, D.G. Wang, J.X. Yang, M.R. Li, J. Zhu, X. Zhou, H.X. Han, C. Li, Spatial separation of photogenerated electrons and holes among 010 and 110 crystal facets of BiVO4, Nat. Commun. 4 (2013).

[5] C. Sun, J. Yang, M. Xu, Y. Cui, W. Ren, J. Zhang, H. Zhao, B. Liang, Recent intensification strategies of SnO2-based photocatalysts: A review, Chem. Eng. J. 427 (2022).

[6] J. Shi, J. Zhang, L. Yang, M. Qu, D.-C. Qi, K.H.L. Zhang, Wide bandgap oxide semiconductors: from materials physics to optoelectronic devices, Adv. Mater. 33 (2021) 2006230.

[7] H.H. Kung, Transition metal oxides: surface chemistry and catalysis, Elsevier, 1989.

[8] A.F. Gouveia, L. Gracia, E. Longo, M.A. San-Miguel, J. Andres, Modulating the properties of multifunctional semiconductors by means of morphology: theory meets experiments, Comput. Mater. Sci 188 (2021), 110417.

[9] T. Bak, T.M. Gur, V.K. Sharma, J. Dodson, K.A. Rahman, J. Nowotny, Evidence of low-dimensional surface structures for oxide materials: impact on energy conversion, ACS Appl. Energy Mater. 1 (2018) 6469–6476.

[10] J. Nowotny, Electron probe for unequivocal surface characterization and surface defect engineering of energy materials. example of BaTiO3, Chem. A Eur. J. 124 (2020) 1610–1618.

[11] K.K. Huang, L. Yuan, S.H. Feng, Crystal facet tailoring arts in perovskite oxides, Inorg. Chem. Front. 2 (2015) 965–981.

[12] Y.L. Zhao, W.L. Zhang, B. Yang, J.Q. Liu, X. Chen, X.L. Wang, C.S. Yang, Gas-sensing enhancement methods for hydrothermal synthesized SnO2-based sensors, Nanotechnology 28 (2017).

[13] X. Gao, T. Zhang, An overview: Facet-dependent metal oxide semiconductor gas sensors, Sens. Actuators B: Chem. 277 (2018) 604–633.

[14] Y. Tang, Y. Zhao, H. Liu, Room-Temperature Semiconductor Gas Sensors: Challenges and Opportunities, ACS Sens, (2022).

[15] Y. Yoon, P.L. Truong, D. Lee, S.H. Ko, Metal-oxide nanomaterials synthesis and applications in flexible and wearable sensors, ACS Nanoscience Au 2 (2021) 64–92.

[16] Q. Zhang, H. Li, L. Gan, Y. Ma, D. Golberg, T. Zhai, In situ fabrication and investigation of nanostructures and nanodevices with a microscope, Chem. Soc. Rev. 45 (2016) 2694–2713.

[17] C. Boukouvala, J. Daniel, E. Ringe, Approaches to modelling the shape of nanocrystals, Nano Converg. 8 (2021) 26.

[18] S.O. Kucheyev, T.F. Baumann, P.A. Sterne, Y.M. Wang, T. van Buuren, A. V. Hamza, L.J. Terminello, T.M. Willey, Surface electronic states in three-dimensional SnO2 nanostructures, Phys. Rev. B 72 (2005).

[19] M. Periyasamy, A. Kar, Modulating the properties of SnO2 nanocrystals: morphological effects on structural, photoluminescence, photocatalytic, electrochemical and gas sensing properties, J. Mater. Chem. C 8 (2020) 4604–4635.

[20] D. Manikandan, R. Murugan, Genesis and tuning of ferromagnetism in SnO2 semiconductor nanostructures: Comprehensive review on size, morphology, magnetic properties and DFT investigations, Prog. Mater Sci. 130 (2022).

[21] Y. Masuda, Recent advances in SnO2 nanostructure based gas sensors, Sens. Actuat. B: Chem. 364 (2022).

[22] O. Lupan, L. Chow, G. Chai, H. Heinrich, S. Park, A. Schulte, Growth of tetragonal SnO2 microcubes and their characterization, J. Cryst. Growth 311 (2008) 152–155.

[23] Y. Toku, Y. Togawa, Y. Morita, Y. Ju, Preferential growth of specific crystal planes based on the dimension control of single crystal SnO2 nanobelts, Mater. Lett. 285 (2021).

[24] G. Zhou, X. Wu, L. Liu, X. Zhu, X. Zhu, Y. Hao, P.K. Chu, Facet-controlled synthesis and facet-dependent photocatalytic properties of SnO2 micropolyhedrons, Appl. Surf. Sci. 349 (2015) 798–804.

[25] N. Zhang, Y. Fan, Y. Lu, C. Li, J. Zhou, X. Li, S. Adimi, S. Ruan, Synthesis of au-decorated SnO2 crystallites with exposed (221) facets and their enhanced acetylene sensing properties, Sens. Actuat. B: Chem. 307 (2020).

[26] X. Han, M. Jin, S. Xie, Q. Kuang, Z. Jiang, Y. Jiang, Z. Xie, L. Zheng, Synthesis of tin dioxide octahedral nanoparticles with exposed high-energy 221 facets and enhanced gas-sensing properties, Angew. Chem. Int. Ed. 48 (2009) 9180–9183.

[27] A. Staerz, U. Weimar, N. Barsan, Current state of knowledge on the metal oxide based gas sensing mechanism, Sens. Actuators B Chem. 358 (2022).

[28] H. Chai, Z. Zheng, K. Liu, J. Xu, K. Wu, Y. Luo, H. Liao, M. Debliquy, C. Zhang, Stability of metal oxide semiconductor gas sensors: a review, IEEE Sens. J. 22 (2022) 5470–5481.

[29] N. Barsan, D. Koziej, U. Weimar, Metal oxide-based gas sensor research: how to? Sens. Actuat. B: Chem. 121 (2007) 18–35.

[30] N. Yamazoe, K. Shimanoe, Theory of power laws for semiconductor gas sensors, Sens. Actuat. B: Chem. 128 (2008) 566–573.

[31] J. Zhang, Z. Qin, D. Zeng, C. Xie, Metal-oxide-semiconductor based gas sensors: screening, preparation, and integration, PCCP 19 (2017) 6313–6329.

[32] N. Goel, K. Kunal, A. Kushwaha, M. Kumar, Metal oxide semiconductors for gas sensing, Eng. Rep. (2022).

[33] S. Liu, Z. Cheng, R. Yu, Nematic-type structure of the SnO2(110) surface at room temperature, ChemPhysChem 23 (2022) e202200338.

[34] P.G. Choi, N. Izu, N. Shirahata, Y. Masuda, Fabrication and H(2)-sensing properties of SnO(2) nanosheet gas sensors, ACS Omega 3 (2018) 14592–14596.

[35] P.G. Choi, N. Izu, N. Shirahata, Y. Masuda, SnO2 nanosheets for selective alkene gas sensing, ACS Appl. Nano Mater. 2 (2019) 1820–1827.

[36] P.M. Desimone, F. Schipani, R. Procaccini, D.A. Mirabella, C.M. Aldao, Evaluating the power-law response for tin dioxide nanostructured sensors in the presence of oxygen and reducing gases, Sens. Actuat. B: Chem. 370 (2022).

[37] M. Li, H. Zhu, G. Wei, A. He, Y. Liu, VOCs gas sensing properties on SnO2 (110) surface with dissociated oxygen species pre-adsorbed: experiments and DFT analysis, J. Mater. Sci. Mater. Electron. 30 (2019) 19625–19638.

[38] L. Zhao, X. Gong, W. Tao, T. Wang, P. Sun, F. Liu, X. Liang, F. Liu, Y. Wang, G. Lu, Understanding the increasing trend of sensor signal with decreasing oxygen partial pressure by a sensing-reaction model based on O(2-) species, ACS Sens 7 (2022) 1095–1104.

[39] L. Zhao, X. Gong, W. Tao, T. Wang, P. Sun, F. Liu, X. Liang, F. Liu, Y. Wang, G. Lu, Understanding the increasing trend of sensor signal with decreasing oxygen partial pressure by a sensing-reaction model based on O2– species, ACS Sens. 7 (2022) 1095–1104.

[40] Y. Kong, Y. Li, X. Cui, L. Su, D. Ma, T. Lai, L. Yao, X. Xiao, Y. Wang, SnO2 nanostructured materials used as gas sensors for the detection of hazardous and flammable gases: a review, Nano Mater. Sci. 4 (2022) 339–350.

[41] A. Gurlo, R. Riedel, In situ and operando spectroscopy for assessing mechanisms of gas sensing, Angew. Chem. Int. Ed. 46 (2007) 3826–3848.

[42] Y.H. Ochoa, F. Schipani, C.M. Aldao, M.A. Ponce, R. Savu, J.E. Rodríguez-Páez, Electrical behavior of BaSnO3 bulk samples formed by slip casting: effect of synthesis methods used for obtaining the ceramic powders, Mater. Res. Bull. 78 (2016) 172–178.

[43] J. Zhang, J. Guo, H. Xu, B. Cao, Reactive-template fabrication of porous SnO2 nanotubes and their remarkable gas-sensing performance, ACS Appl. Mater. Inter. 5 (2013) 7893–7898.

[44] K. Awa, R. Akashi, A. Akita, S.-I. Naya, H. Kobayashi, H. Tada, Highly efficient and selective oxidation of ethanol to acetaldehyde by a hybrid photocatalyst consisting of SnO2 nanorod and rutile TiO2 with heteroepitaxial junction, ChemPhysChem 20 (2019) 2155–2161.

[45] G. Pang, H. Jin, Y. Li, Q. Wan, Y. Sun, S. Feng, A. Gedanken, Preparation and spectroscopy study of monodispersed metal oxide nanocrystals, J. Mater. Sci. 41 (2006) 1429–1431.

[46] S. Mathur, S. Barth, H. Shen, J.C. Pyun, U. Werner, Size-dependent photoconductance in SnO2 nanowires, Small 1 (2005) 713–717.

[47] J.B. Zhang, X.N. Li, S.L. Bai, R.X. Luo, A.F. Chen, Y. Lin, High-yield synthesis of SnO2 nanobelts by water-assisted chemical vapor deposition for sensor applications, Mater. Res. Bull. 47 (2012) 3277–3282.

[48] D.S. Kolokolov, A.A. Podurets, V.D. Nikonova, P.N. Vorontsov-Velyaminov, N. P. Bobrysheva, M.G. Osmolowsky, O.M. Osmolovskaya, M.A. Voznesenskiy, SnO2 nanoparticles with different aspect ratio and structural parameters: fabrication, photocatalytic efficiency dependences and fast organic dyes degradation, Appl. Surf. Sci. 599 (2022).

[49] M. Aslam, M.T. Qamar, S. Ali, A.U. Rehman, M.T. Soomro, I. Ahmed, I.M.I. Ismail, A. Hameed, Evaluation of SnO2 for sunlight photocatalytic decontamination of water, J. Environ. Manage. 217 (2018) 805–814.

[50] M. Batzill, Surface science studies of gas sensing materials: SnO2, Sensors 6 (2006) 1345–1366.

[51] A. Beltrán, J. Andrés, E. Longo, E.R. Leite, Thermodynamic argument about SnO2 nanoribbon growth, Appl. Phys. Lett. 83 (2003) 635–637.

[52] E.R. Leite, T.R. Giraldi, F.M. Pontes, E. Longo, A. Beltrán, J. Andrés, Crystal growth in colloidal tin oxide nanocrystals induced by coalescence at room temperature, Appl. Phys. Lett. 83 (2003) 1566–1568.

[53] S. Sain, A. Kar, A. Patra, S.K. Pradhan, Structural interpretation of SnO2 nanocrystals of different morphologies synthesized by microwave irradiation and hydrothermal methods, CrstEngComm 16 (2014) 1079–1090.

[54] S. Singkammo, A. Wisitsoraat, C. Sriprachuabwong, A. Tuantranont, S. Phanichphant, C. Liewhiran, Electrolytically exfoliated graphene-loaded flame-made Ni-doped SnO2 composite film for acetone sensing, ACS Appl. Mater. Inter. 7 (2015) 3077–3092.

[55] H. Zakaryan, V. Aroutiounian, CO gas adsorption on SnO2 surfaces: density functional theory study, Sens. Transducers 212 (2017) 50–56.

[56] C. Jiang, G. Zhang, Y. Wu, L. Li, K. Shi, Facile synthesis of SnO2 nanocrystalline tubes by electrospinning and their fast response and high sensitivity to NOx at room temperature, CrstEngComm 14 (2012) 2739–2747.

[57] F.c.R. Sensato, R. Custódio, M. Calatayud, A. Beltrán, J. Andrés, J.R. Sambrano, E. Longo, Periodic study on the structural and electronic properties of bulk, oxidized and reduced SnO2(110) surfaces and the interaction with O2, Surf. Sci., 511 (2002) 408-420.

[58] D.G. Stroppa, L.A. Montoro, A. Beltrán, T.G. Conti, R.O. da Silva, J. Andrés, E. Longo, E.R. Leite, A.J. Ramirez, Unveiling the chemical and morphological features of Sb−SnO2 nanocrystals by the combined use of high-resolution transmission electron microscopy and ab initio surface energy calculations, J. Am. Chem. Soc. 131 (2009) 14544–14548.

[59] A.A. Abokifa, K. Haddad, J. Fortner, C.S. Lo, P. Biswas, Sensing mechanism of ethanol and acetone at room temperature by SnO2 nano-columns synthesized by aerosol routes: theoretical calculations compared to experimental results, J. Mater. Chem. A 6 (2018) 2053–2066.

[60] H. Feng, C. Li, T. Li, F. Diao, T. Xin, B. Liu, Y. Wang, Three-dimensional hierarchical SnO2 dodecahedral nanocrystals with enhanced humidity sensing properties, Sens. Actuat. B: Chem. 243 (2017) 704–714.

[61] Z. Lu, D. Ma, L. Yang, X. Wang, G. Xu, Z. Yang, Direct CO oxidation by lattice oxygen on the SnO2(110) surface: a DFT study, PCCP 16 (2014) 12488–12494.

[62] M. Habgood, N. Harrison, An ab initio study of oxygen adsorption on tin dioxide, Surf. Sci. 602 (2008) 1072–1079.

[63] S. Kucharski, C. Blackman, Atomic Descriptions of Gas-Surface Interactions on Tin Dioxide, in: Chemosensors, 2021.

[64] K.V. Sopiha, O.I. Malyi, C. Persson, P. Wu, Chemistry of Oxygen Ionosorption on SnO(2) Surfaces, ACS Appl. Mater. Interfaces 13 (2021) 33664–33676.

[65] A. Gurlo, Nanosensors: does crystal shape matter? Small 6 (2010) 2077–2079.

[66] A. Gurlo, Nanosensors: towards morphological control of gas sensing activity. SnO2, In2O3, ZnO and WO3 case studies, Nanoscale 3 (2011) 154–165.

[67] J.-M. Ducéré, A. Hemeryck, A. Estève, M.D. Rouhani, G. Landa, P. Ménini, C. Tropis, A. Maisonnat, P. Fau, B. Chaudret, A computational chemist approach to gas sensors: modeling the response of SnO2 to CO, O2, and H2O Gases, J. Comput. Chem. 33 (2012) 247–258.

[68] A. Gurlo, Interplay between O2 and SnO2: oxygen ionosorption and spectroscopic evidence for adsorbed oxygen, ChemPhysChem 7 (2006) 2041–2052.

[69] N. Barsan, C. Simion, T. Heine, S. Pokhrel, U. Weimar, Modeling of sensing and transduction for p-type semiconducting metal oxide based gas sensors, J. Electroceram. 25 (2010) 11–19.

[70] D. Degler, S. Wicker, U. Weimar, N. Barsan, Identifying the active oxygen species in SnO2 based gas sensing materials: an operando IR spectrsocopy study, J. Phys. Chem. C 119 (2015) 11792–11799.

[71] M. Anpo, G. Costentin, E. Giamello, H. Lauron-Pernot, Z. Sojka, Characterisation and reactivity of oxygen species at the surface of metal oxides, J. Catal. 393 (2021) 259–280.

[72] C. Salvini, M. Re Fiorentin, F. Risplendi, F. Raffone, G. Cicero, Active surface structure of SnO2 catalysts for CO2 reduction revealed by ab initio simulations, J. Phys. Chem. C 126 (2022) 14441–14447.

[73] Y. Xiong, Y. Lin, X. Wang, Y. Zhao, J. Tian, Defect engineering on SnO2 nanomaterials for enhanced gas sensing performances, Adv. Powder Technol. 1 (2022).

[74] Y. Yuan, Y. Wang, M. Wang, J. Liu, C. Pei, B. Liu, H. Zhao, S. Liu, H. Yang, Effect of unsaturated Sn atoms on gas-sensing property in hydrogenated SnO(2) nanocrystals and sensing mechanism, Sci. Rep. 7 (2017) 1231.

[75] J. Andrés, L. Gracia, A.F. Gouveia, M.M. Ferrer, E. Longo, Effects of surface stability on the morphological transformation of metals and metal oxides as investigated by first-principles calculations, Nanotechnology 26 (2015) 405703–405713.

[76] M.M. Ferrer, A.F. Gouveia, L. Gracia, E. Longo, J. Andres, A 3D platform for the morphology modulation of materials: First principles calculations on the thermodynamic stability and surface structure of metal oxides: Co3O4, α-Fe2O3, and In2O3, Model. Simul. Mater. Sci. Eng. 24 (2016) 025007–025016.

[77] A.F. Gouveia, M.M. Ferrer, J.R. Sambrano, J. Andres, E. Longo, Modeling the atomic-scale structure, stability, and morphological transformations in the tetragonal phase of LaVO4, Chem. Phys. Lett. 660 (2016) 87–92.

[78] A.F. Gouveia, M. Assis, L.S. Cavalcante, L. Gracia, E. Longo, J. Andres, Reading at exposed surfaces: theoretical insights into photocatalytic activity of ZnWO4, Front. Res. Today 1 (2018).

[79] A.H. Pinto, A.E. Nogueira, C.J. Dalmaschio, I.N. Frigini, J.C. de Almeida, M.M. Ferrer, O.M. Berengue, R.A. Gonçalves, V.R. de Mendonça, Doped Tin Dioxide (d-SnO2) and Its Nanostructures: Review of the Theoretical Aspects, Photocatalytic and Biomedical Applications, in: Solids, 2022, pp. 327-360.

[80] H.J. Queisser, E.E. Haller, Defects in semiconductors: some fatal, some vital, Science 281 (1998) 945–950.

[81] R. Waser, M. Aono, Nanoionics-based resistive switching memories, Nature Mater. 6 (2007) 833–840.

[82] R.A. De Souza, Oxygen diffusion in SrTiO3 and related perovskite oxides, Adv. Funct. Mater. 25 (2015) 6326–6342.

[83] A. Alkauskas, M.D. McCluskey, C.G. Van de Walle, Tutorial: defects in semiconductors—combining experiment and theory, J. Appl. Phys. 119 (2016), 181101.

[84] F. Gunkel, D.V. Christensen, Y.Z. Chen, N. Pryds, Oxygen vacancies: the (in) visible friend of oxide electronics, Appl. Phys. Lett. 116 (2020), 120505.

[85] M.D. McCluskey, A. Janotti, Defects in semiconductors, J. Appl. Phys. 127 (2020), 190401.

[86] C.E. Macchi, Nanostructures subsurface characterization using positron annihilation spectroscopy, Materia-Rio De Janeiro 18 (2013) 1425–1435.

[87] G. Kresse, J. Furthmuller, Efficiency of ab-initio total energy calculations for metals and semiconductors using a plane-wave basis set, Comput. Mater. Sci 6 (1996) 15–50.

[88] G. Kresse, J. Furthmuller, Efficient iterative schemes for ab initio total-energy calculations using a plane-wave basis set, Phys. Rev. B: Condens. Matter Mater. Phys. 54 (1996) 11169–11186.

[89] G. Kresse, D. Joubert, From ultrasoft pseudopotentials to the projector augmented-wave method, Phys. Rev. B: Condens. Matter Mater. Phys. 59 (1999) 1758–1775.

[90] G. Kresse, J. Hafner, Ab initio molecular-dynamics for liquid-metals, Phys. Rev. B 47 (1993) 558–561.

[91] J.P. Perdew, J.A. Chevary, S.H. Vosko, K.A. Jackson, M.R. Pederson, D.J. Singh, C. Fiolhais, Atoms, molecules, solids and surfaces - applications of the generalized gradient approximation for exchange and correlation, Phys. Rev. B 46 (1992) 6671–6687.

[92] J.P. Perdew, K. Burke, M. Ernzerhof, Generalized gradient approximation made simple, Phys. Rev. Lett. 77 (1996) 3865–3868.

[93] P.E. Blochl, Projector augmented-wave method, Phys. Rev. B 50 (1994) 17953–17979.

[94] G.D. Barmparis, Z. Lodziana, N. Lopez, I.N. Remediakis, Nanoparticle shapes by using Wulff constructions and first-principles calculations, Beilstein J. Nanotechnol. 6 (2015) 361–368.

[95] O. Lupan, L. Chow, G. Chai, H. Heinrich, S. Park, A. Schulte, Synthesis of one-dimensional SnO2 nanorods via a hydrothermal technique, Physica E Low Dimens. Syst. Nanostruct. 41 (2009) 533–536.

[96] J. Oviedo, M.J. Gillan, Energetics and structure of stoichiometric SnO2 surfaces studied by first-principles calculations, Surf. Sci. 463 (2000) 93–101.

[97] P.A. Mulheran, J.H. Harding, The stability of SnO2 surfaces, Model. Simul. Mater. Sci. Eng. 1 (1992) 39.

[98] B. Slater, C.R.A. Catlow, D.H. Gay, D.E. Williams, V. Dusastre, Study of surface segregation of antimony on SnO2 surfaces by computer simulation techniques, J. Phys. Chem. B 103 (1999) 10644–10650.

[99] F.A. Selim, Positron annihilation spectroscopy of defects in nuclear and irradiated materials- a review, Mater Charact 174 (2021), 110952.

[100] F. Tuomisto, I. Makkonen, Defect identification in semiconductors with positron annihilation: experiment and theory, Rev. Mod. Phys. 85 (2013) 1583–1631.

[101] R.S. Brusa, S. Mariazzi, L. Ravelli, P. Mazzoldi, G. Mattei, W. Egger, C. Hugenschmidt, B. Lowe, P. Pikart, C. Macchi, A. Somoza, Study of defects in implanted silica glass by depth profiling positron Annihilation Spectroscopy, Nucl. Instrum. Methods Phys. Res. B 268 (2010) 3186–3190.

[102] A. Somoza, C. Macchi, R. Romero, Thermal generation of point defects in beta Cu-Zn-Al alloys, in: Y.C. Jean, M. Eldrup, D.M. Schrader, R.N. West (Eds.) Positron Annihilation: Icpa-11 - Proceedings of the 11th International Conference on Positron Annihilation, Kansas City, Missouri, USA, May 1997, 1997, pp. 587-589.

[103] C. Macchi, A. Somoza, A. Dupasquier, A.L. Garcia, M. Castro, Positron trapping in BaTiO3 perovskite, J. Phys. Condens. Matter 13 (2001) 5717–5722.

[104] C. Macchi, A. Somoza, J. Guimpel, S. Suarez, W. Egger, C. Hugenschmidt, S. Mariazzi, R.S. Brusa, Oxygen related defects and vacancy clusters identified in sputtering grown UOx thin films by positron annihilation techniques, Results Phys. 27 (2021).

[105] M.A. Ponce, C. Macchi, F. Schipani, C.M. Aldao, A. Somoza, Mild degradation processes in ZnO-based varistors: the role of Zn vacancies, Phil. Mag. 95 (2015) 730–743.

[106] M. Assis, M.A. Ponce, A.F. Gouveia, D. Souza, J. da Costa, V. Teodoro, Y. G. Gobato, J. Andres, C. Macchi, A. Somoza, E. Longo, Revealing the nature of defects in alpha-Ag2WO4 by positron annihilation lifetime spectroscopy: a joint experimental and theoretical study, Cryst. Growth Des. 21 (2021) 1093–1102.

[107] I. Makkonen, E. Korhonen, V. Prozheeva, F. Tuomisto, Identification of vacancy defect complexes in transparent semiconducting oxides ZnO, In2O3 and SnO2, J. Phys. Condens. Matter 28 (2016), 224002.

[108] C.H. Shek, J.K.L. Lai, G.M. Lin, Investigation of interface defects in nanocrystalline SnO2 by positron annihilation, J. Phys. Chem. Solid 60 (1999) 189–193.

[109] P.R. Guagliardo, E.R. Vance, Z. Zhang, J. Davis, J.F. Williams, S.N. Samarin, Positron annihilation lifetime studies of Nb-Doped TiO2, SnO2, and ZrO2, J. Am. Ceram. Soc. 95 (2012) 1727–1731.

[110] C. Macchi, M.A. Ponce, P.M. Desimone, C.M. Aldao, A. Somoza, Vacancy-like defects in nanocrystalline SnO2: influence of the annealing treatment under different atmospheres, Phil. Mag. 98 (2018) 673–692.

[111] Y. Shen, W. Wang, A. Fan, D. Wei, W. Liu, C. Han, Y. Shen, D. Meng, X. San, Highly sensitive hydrogen sensors based on SnO2 nanomaterials with different morphologies, Int. J. Hydrog. Energy 40 (2015) 15773–15779.

[112] R. Xu, L.-X. Zhang, M.-W. Li, Y.-Y. Yin, J. Yin, M.-Y. Zhu, J.-J. Chen, Y. Wang, L.-J. Bie, Ultrathin SnO2 nanosheets with dominant high-energy 001 facets for low temperature formaldehyde gas sensor, Sens. Actuators B: Chem. 289 (2019) 186–194.

[113] L. Xing, Y. Dong, X. Wu, SnO2 nanoparticle photocatalysts for enhanced photocatalytic activities, Mater. Res. Express 5 (2018).

[114] A. Kar, J. Olszówka, S. Sain, S.-R.-I. Sloman, O. Montes, A. Fernández, S. K. Pradhan, A.E.H. Wheatley, Morphological effects on the photocatalytic properties of SnO2 nanostructures, J. Alloy. Compd. 810 (2019).

[115] B. Cheng, J.M. Russell, W.S. Shi, L. Zhang, E.T. Samulski, Large-scale, solution-phase growth of single-crystalline SnO2 nanorods, J. Am. Chem. Soc. 126 (2004) 5972–5973.

[116] E.R. Leite, C. Ribeiro, Oriented Attachment and Mesocrystals, in: E.R. Leite, C. Ribeiro (Eds.) Crystallization and Growth of Colloidal Nanocrystals, Springer New York, New York, NY, 2012, pp. 45-68.

[117] R. Deshmukh, M. Niederberger, Mechanistic aspects in the formation, growth and surface functionalization of metal oxide nanoparticles in organic solvents, Chem Eur J 23 (2017) 8542–8570.

[118] C.J. Dalmaschio, C. Ribeiro, E.R. Leite, Impact of the colloidal state on the oriented attachment growth mechanism, Nanoscale 2 (2010) 2336–2345.

[119] D.G. Stroppa, L.A. Montoro, A. Beltrán, T.G. Conti, R.O. da Silva, J. Andrés, E. R. Leite, A.J. Ramirez, Anomalous oriented attachment growth behavior on SnO2 nanocrystals, Chem. Commun. 47 (2011) 3117–3119.

[120] D.G. Stroppa, L.A. Montoro, A. Beltrán, T.G. Conti, R.O. da Silva, J. Andrés, E. R. Leite, A.J. Ramirez, Dopant segregation analysis on Sb:SnO2 nanocrystals, Chem. – Eur. J. 17 (2011) 11515–11519.

[121] S. Maya-Johnson, L. Gracia, E. Longo, J. Andres, E.R. Leite, Synthesis of cuboctahedral CeO2 nanoclusters and their assembly into cuboid nanoparticles by oriented attachment, ChemNanoMat 3 (2017) 228–232.

[122] N.G. Macedo, A.F. Gouveia, R.A. Roca, M. Assis, L. Gracia, J. Andrés, E.R. Leite, E. Longo, Surfactant-mediated morphology and photocatalytic activity of α-Ag2WO4 material, J. Phys. Chem. C 122 (2018) 8667–8679.

[123] L.O. Laier, M. Assis, C.C. Foggi, A.F. Gouveia, C.E. Vergani, L.C.L. Santana, L. S. Cavalcante, J. Andres, E. Longo, Surface-dependent properties of alpha-Ag2WO4: a joint experimental and theoretical investigation, Theor. Chem. Acc. 139 (2020) 108.

[124] J. Ma, N. Xu, Y. Luo, Q. Liu, Y. Pu, Defect generation and morphology transformation mechanism of CeO2 particles prepared by molten salt method, Ceram. Int. (2022).

[125] V. Teodoro, A.F. Gouveia, T.R. Machado, A.B. Trench, N. Jacomaci, M. Assis, G. E. Marques, M.D. Teodoro, M.A. San-Miguel, J. Andrés, J. Bettini, E. Longo, Connecting morphology and photoluminescence emissions in β-Ag2MoO4 microcrystals, Ceram. Int. 48 (2022) 3740–3750.

[126] L.L. Liu, E. Nakouzi, M.L. Sushko, G.K. Schenter, C.J. Mundy, J. Chun, J.J. De Yoreo, Connecting energetics to dynamics in particle growth by oriented attachment using real-time observations, Nat. Commun. 11 (2020).

[127] C.Y. Dong, Y. Zhou, N. Ta, W.J. Shen, Formation mechanism and size control of ceria nanocubes, CrstEngComm 22 (2020) 3033–3041.

[128] K. Kim, D. Jeong, S. Lee, M. Bae, J. Bae, W. Jung, J.W. Han, A simple descriptor to rapidly screen CO oxidation activity on rare-earth metal-doped CeO2: from experiment to first-principles, ACS Appl. Mater. Inter. 9 (2017) 15449–15458.

[129] Y. Masuda, Facet controlled growth mechanism of SnO(2) (101) nanosheet assembled film via cold crystallization, Sci. Rep. 11 (2021) 11304.